

# Single-Crystal Permanent Magnets: Extraordinary Magnetic Behavior in the Ta-, Cu-, and Fe-Substituted CeCo<sub>5</sub> Systems


Tej N. Lamichhane,<sup>1,2</sup> Michael T. Onyszczyk,<sup>2</sup> Olena Palasyuk,<sup>1,3</sup> Saba Sharikadze,<sup>2</sup> Tae-Hoon Kim,<sup>1</sup> Qisheng Lin,<sup>1</sup> Matthew J. Kramer,<sup>1,3</sup> R.W. McCallum,<sup>1</sup> Aleksander L. Wysocki,<sup>1</sup> Manh Cuong Nguyen,<sup>1</sup> Vladimir P. Antropov,<sup>1</sup> Tribhuwan Pandey,<sup>4</sup> David Parker,<sup>4</sup> Sergey L. Bud'ko,<sup>1,2</sup> Paul C. Canfield,<sup>1,2</sup> and Andriy Palasyuk<sup>1,\*</sup>

<sup>1</sup>*The Ames Laboratory, U.S. Department of Energy, Iowa State University, Ames, Iowa 50011, USA*

<sup>2</sup>*Department of Physics and Astronomy, Iowa State University, Ames, Iowa 50011, USA*

<sup>3</sup>*Department of Material Science and Engineering, Iowa State University, Ames, Iowa 50011, USA*

<sup>4</sup>*Oak Ridge National Laboratory, Oak Ridge, Tennessee 37831, USA*

 (Received 23 May 2018; revised manuscript received 23 November 2018; published 25 January 2019)

To reduce material and processing costs of commercial permanent magnets and to attempt to fill the empty niche of energy products, 10–20 MGOe, between low-flux (ferrites, alnico) and high-flux (Nd<sub>2</sub>Fe<sub>14</sub>B- and SmCo<sub>5</sub>-type) magnets, we report the synthesis, structure, magnetic properties, and modeling of Ta-, Cu-, and Fe-substituted CeCo<sub>5</sub>. Using a self-flux technique, we grow single crystals of Ce<sub>15.1</sub>Ta<sub>1.0</sub>Co<sub>74.4</sub>Cu<sub>9.5</sub>, Ce<sub>16.3</sub>Ta<sub>0.6</sub>Co<sub>68.9</sub>Cu<sub>14.2</sub>, Ce<sub>15.7</sub>Ta<sub>0.6</sub>Co<sub>67.8</sub>Cu<sub>15.9</sub>, Ce<sub>16.3</sub>Ta<sub>0.3</sub>Co<sub>61.7</sub>Cu<sub>21.7</sub>, and Ce<sub>14.3</sub>Ta<sub>1.0</sub>Co<sub>62.0</sub>Fe<sub>12.3</sub>Cu<sub>10.4</sub>. X-ray-diffraction analysis shows that these materials retain a CaCu<sub>5</sub> substructure and incorporate small amounts of Ta in the form of “dumbbells,” filling the 2*e* crystallographic sites within the one-dimensional hexagonal channel with the 1*a* Ce site, whereas Co, Cu, and Fe are statistically distributed among the 2*c* and 3*g* crystallographic sites. Scanning-electron-microscopy, energy-dispersive-x-ray-spectroscopy, and scanning-transmission-electron-microscopy examinations provide strong evidence of the single-phase nature of the as-grown crystals, even though they readily exhibit significant magnetic coercivities of approximately 1.6 kOe to approximately 1.8 kOe caused by Co-enriched, nanosized structural defects and faults that can serve as pinning sites. Heat treatments at 1040 °C for 10 h and hardening at 400 °C for 4 h lead to the formation of a so-called composite crystal with a bimodal microstructure that consists of a Ta-poor matrix and Ta-rich laminal precipitates. Formation of the composite crystal during the heat treatment creates a three-dimensional array of extended defects within a primarily single-grain single crystal, which greatly improves its magnetic characteristics. Possible causes for the formation of the composite crystal may be associated with Ta atoms leaving matrix interstices at lower temperatures and/or matrix degradation induced by decreased miscibility at lower temperatures. Fe strongly increases both the Curie temperature and magnetization of the system resulting, in  $(BH)_{\max} \approx 13$  MGOe at room temperature.

DOI: [10.1103/PhysRevApplied.11.014052](https://doi.org/10.1103/PhysRevApplied.11.014052)

## I. INTRODUCTION

To find new economical alternatives to commercial, high-flux permanent magnets, we focus on the Ta-, Cu-, and Fe-substituted CeCo<sub>5</sub> system (CaCu<sub>5</sub>-type structure), which, unlike typical commercial magnetic grades with critical rare earths (Nd, Sm, Dy, etc.), uses widely available and more-affordable Ce [1–3]. The incorporation of Ce, instead of critical elements, into magnets may significantly reduce the price and supply-chain dependence of commercial magnets. Despite the mixed Ce<sup>3+</sup>/Ce<sup>4+</sup> valency problem, which is typically adverse for the magnetocrystalline

anisotropy, recent experimental studies on the Nd<sub>2</sub>Fe<sub>14</sub>B (2:14:1) system showed that Ce substitutes can compete with commercial high-flux grades at lower material costs [4–7]. Similarly, studies on the Ce-containing SmCo<sub>5</sub> (1:5) and Sm<sub>2</sub>Co<sub>17</sub> (2:17) systems showed that satisfactory cost-to-performance balances suitable for modern rare-earth criticalities and market demands are expected [8–11]. Therefore, we believe that Cu- and Fe-substituted CeCo<sub>5</sub> systems require a new and deeper examination [12–14]. After being understood and optimized, these Ce-based systems may compete on the levels of both material-processing cost and properties as so-called gap magnets, performing in the gap of magnetic energies, between 10 and 20 MGOe, which currently exists between the

\*palasyuk@ameslab.gov

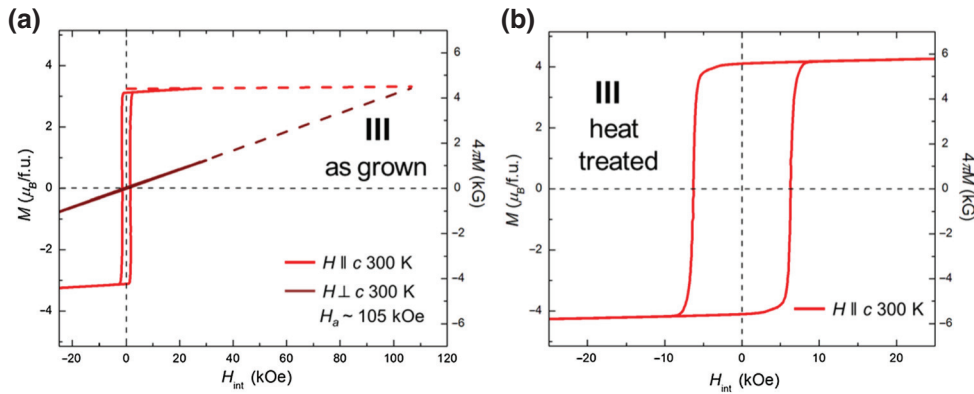


FIG. 1. (a) Anisotropic field-dependent magnetization of as-grown  $\text{Ce}_{15.7}\text{Ta}_{0.6}\text{Co}_{67.8}\text{Cu}_{15.9}$  (III) at 300 K for applied field along and perpendicular to the crystallographic axis. The inferred anisotropy field,  $H_a$ , is also shown. (b) After heat treatment, the magnetic hysteresis loop of the same sample along the easy magnetization axis (i.e., the crystallographic  $c$  axis). f.u., formula unit.

rare-earth-free alnico and ferrite grades and the sintered 1:5 and 2:14:1 magnetic grades, which contain critical rare earths [15].

Despite previous extensive explorations, the intrinsic properties of the  $\text{CeCo}_5$  system have not been fully or systematically established [13,14,16–36], and the metallurgy related to the magnetic pinning/coercivity mechanism is not fully understood. Although anisotropy characterization is best obtained from single crystals, single-crystal-growth reports in Cu- or Fe-substituted  $\text{CeCo}_5$  systems are scarce and limited to several Bridgman-type attempts [21,22] for compositions of approximately  $\text{CeCo}_{3.5}\text{Fe}_{0.5}\text{Cu}$  [37].

In this paper we report the successful self-flux growth [38,39] of five representatives of Ta-, Cu-, and Fe-substituted  $\text{CeCo}_5$  followed by characterization of their structural and magnetic properties. We study the phenomenon of pronounced magnetic coercivity in the “as-grown” crystals and its further development during heat treatment as illustrated in Fig. 1. Subgrain phase segregation creates the necessary conditions for magnetic domain pinning. We also discuss the possible ways to improve, manipulate, and control the system in an attempt to improve its magnetic characteristics in conjunction with first-principles density-functional-theory (DFT) calculations and multiscale modeling.

## II. EXPERIMENTAL PROCEDURES

### A. Synthesis

Single crystals are grown via the solution growth method [38,39]. The reaction metals [Ce (99.99%) and Cu (99.95%) from Ames Laboratory MPC and Co (99.95%) from Alfa Aesar] are placed into three-capped Ta containers [40] welded under an Ar atmosphere, which are then sealed into fused-silica tubes and placed in a high-temperature box furnace. The furnace is heated from near room temperature to  $900^\circ\text{C}$  over 3 h, held at  $900^\circ\text{C}$  for 3 h, heated to  $1200^\circ\text{C}$  over 3 h, and held at  $1200^\circ\text{C}$  for 10 h. The furnace is then cooled to  $1070^\circ\text{C}$  over 75 h. At  $1070^\circ\text{C}$  the excess flux is decanted by centrifugation [38,39]. Decanting occurs as the centrifuge accelerates

from rest toward an 8500 revolutions/min set point. The exact temperature profile of the growths and pictures of the typical crystals are presented in Fig. 2.

### B. Heat treatment

After growth, some single crystals undergo identical, two-stage heat treatments performed in a Dentsply Ceramico (Vulcan 3 series) multistage programmable furnace, which includes dwelling at  $1040^\circ\text{C}$  for 10 h, then cooling at a rate of  $10^\circ\text{C}/\text{min}$  to  $400^\circ\text{C}$ , followed by dwelling at this temperature for the next 8 h with a subsequent furnace cool to room temperature. We based this schedule on literature reports [19,21,26–30]. Different Cu contents may require slightly different temperature and time parameters for the best final magnetic characteristics, but the optimization of the heat-treatment procedure is a subject of ongoing work.

### C. Metallography and scanning-electron-microscopy–energy-dispersive-x-ray-spectroscopy analysis

Samples for metallographic examination are placed in approximately-1-in.-diameter epoxy-resin pucks and are

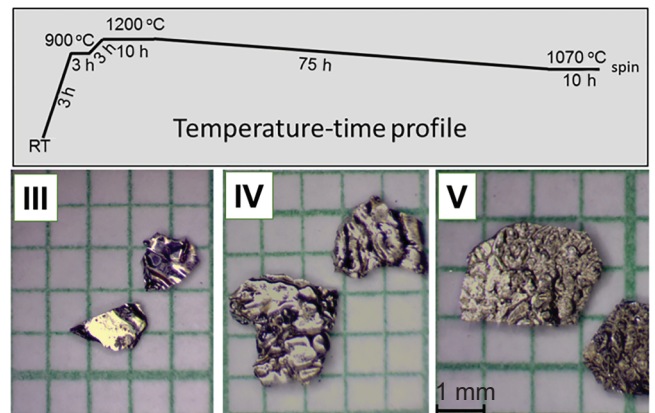


FIG. 2. Temperature-time profile used for single-crystal growth and general appearance of self-flux-grown platelike crystals of  $\text{Ce}_{15.7}\text{Ta}_{0.6}\text{Co}_{67.8}\text{Cu}_{15.9}$  (III),  $\text{Ce}_{16.3}\text{Ta}_{0.3}\text{Co}_{61.7}\text{Cu}_{21.7}$  (IV), and  $\text{Ce}_{14.3}\text{Ta}_{1.0}\text{Co}_{62.0}\text{Fe}_{12.3}\text{Cu}_{10.4}$  (V) (for details see Table I).

TABLE I. Composition of single crystals (with standard deviation) and their lattice parameters as grown (AG) and after the heat treatment (HT). The lattice parameters and corresponding errors are derived from the Rietveld fits.

Compound	EDS composition (at. %)										Lattice parameters	
	Ce		Ta <sup>a</sup>		Co		Fe		Cu		$a, c$ (Å); $V$ (Å <sup>3</sup> ) <sup>b</sup>	
	AG	HT	AG	HT	AG	HT	AG	HT	AG	HT	AG	HT
<b>I</b>	15.1(1)	16.1(1)	1.0	0.6	74.4(2)	73.6(2)	...	...	9.5(1)	9.8(1)	4.912(1)	4.921(1)
											4.045(1)	4.031(1)
											84.52(1)	84.58(2)
<b>II</b>	16.3(1)	16.2(1)	0.6	0.4	68.9(2)	69.4(2)	...	...	14.2(1)	14.0(1)	4.933(1)	4.933(1)
											4.031(1)	4.028(1)
											84.95(2)	84.90(2)
<b>III</b>	15.7(1)	15.8(1)	0.6	0.1	67.8(2)	67.1(2)	...	...	15.9(1)	17.1(1)	4.943(1)	4.944(1)
											4.032(1)	4.028(1)
											85.31(1)	85.26(1)
<b>IV</b>	16.3(1)	16.5(1)	0.3	0.05	61.7(2)	61.9(2)	...	...	21.7(1)	21.6(1)	4.950(1)	4.954(1)
											4.033(1)	4.028(1)
											85.57(2)	85.61(2)
<b>V</b>	14.3(1)	13.9(1)	1.0	0.2	62.0(2)	62.7(2)	12.3(1)	13.0(1)	10.4(1)	10.2(1)	4.922(1)	4.924(1)
											4.075(1)	4.071(1)
											85.50(2)	85.48(2)

Heat treatment is as follows: 1040 °C (10 h) followed by cooling at 10 °C/min to 400 °C (8 h).

<sup>a</sup>Standard deviations for Ta range from 0.02 to 0.05 at. %.

<sup>b</sup>Space group  $P6/mmm$ .

polished with various grits of silicon carbide followed by a glycol-based, fine, polycrystalline, diamond suspension. Platelike single crystals (Fig. 2) are mounted with their plates parallel to the polishing surface to allow characterization along planes perpendicular to the crystal [001] direction. Imaging studies of single-crystal samples are performed with an FEI Teneo field-emission scanning electron microscope. Their compositions are determined via energy-dispersive x-ray spectra obtained with an Oxford Instruments energy-dispersive-spectroscopy (EDS) and electron-backscatter-diffraction module averaging over three to five regions on their metallographically prepared surfaces (see Table I).

#### D. Transmission-electron-microscopy characterization

Cross sections from single-crystal  $Ce_{15.7}Ta_{0.6}Co_{67.8}Cu_{15.9}$  (**III**) are prepared with a dual-beam focused-ion-beam system (FEI Helios NanoLab G3 UC) with a lift-out approach. To reduce surface damage sustained during Ga-ion milling, the final thinning and cleaning steps are conducted with 5 and 2 kV for 5 min. The transmission-electron-microscopy (TEM) analysis is performed with a Titan Themis (FEI) probe Cs-corrected transmission electron microscope equipped with a Super-X EDS detector to characterize microstructure and elemental distribution.

#### E. Powder and single-crystal x-ray diffraction

Polycrystalline powders are obtained by our crushing the sample with an agate mortar and pestle. X-ray powder

diffraction data are collected from the as-grown and heat-treated crystals. The measurements are performed with PANalytical X-Pert Pro (Co  $K\alpha$  radiation,  $\lambda = 1.78897$  Å) and a Bruker D8 Advance (Cu  $K\alpha$  radiation,  $\lambda = 1.54056$  Å) diffraction systems. Powdered samples are evenly dispersed on a zero-background Si holder with the aid of a small quantity of vacuum grease. Diffraction scans are taken in the  $\theta/2\theta$  mode with the following parameters:  $2\theta$  region,  $20^\circ$ – $110^\circ$ ; step scan,  $0.02^\circ$ ; counting time per step, 60 s. The FullProf Suite program package [41] is used for Rietveld refinement of the crystal structures.

Single-crystal diffraction data are collected at room temperature with a Bruker SMART APEX II diffractometer (Mo  $K\alpha$  radiation) equipped with a CCD area detector. Four sets of 360 frames with  $0.5^\circ$  scans in  $\omega$  and exposure times of 10–15 s per frame are collected. The reflection intensities are integrated with use of the subprogram SAINT in the SMART software package [42]. The space group is determined with the program XPREP and the SHELXTL 6.1 software package [43]. Empirical absorption corrections are made with the program SADABS [44]. Finally, each structure is solved by direct methods using SHELXTL 6.1 and refined by full-matrix least squares on  $F_0^2$ , with anisotropic thermal parameters and a secondary extinction parameter. The error bars for lattice-parameter determination by both powder and single-crystal x-ray-diffraction (XRD) methods come from the fits of corresponding data. However, it is anticipated that the instrumental error may be on the order of 0.005 Å. Detailed crystallographic information is presented in Supplemental Material [45].

## F. Measurement of magnetic properties

Magnetic properties are measured with a vibrating-sample magnetometer in a cryogen-free VersaLab physical-property-measurement system (Quantum Design) with magnetic fields up to 3 T and temperatures in the 50–350 K range with use of the standard option and in the 300–1000 K range with use of the oven option. An alumina cement (Zircar) is used to hold the sample on the heater stick for the high-temperature measurements. The demagnetization factors are determined experimentally by the relation  $H_{\text{int}} = H - NM$  [46,47].

## III. STRUCTURE AND COMPOSITION ANALYSIS

The  $\text{Ce}(\text{Co}_{1-x-y}\text{Fe}_x\text{Cu}_y)_5$  system favors slightly Ce deficiency [21–24], and the appearance of transition-metal “dumbbells” may lead to structural transformations toward the 1:7 and 2:17 phases. Therefore, we use approximately 1:5 as the designation for the general description of our reported systems.

### A. SEM-EDS examinations and composition analysis

The SEM backscattered-electron images of the as-grown crystals [Figs. 3(a)–3(c), upper panels] show the uniformity of their approximately (0001) polished surface (even at  $\times 30\,000$  magnification), which suggests a single phase, although small inhomogeneities are shown in Fig. 6 (TEM). Elemental EDS analysis (Table I)

shows the Ce:Co/Cu ratios are close to the 1:5 stoichiometry, with Cu content increasing from approximately 10 at. % to approximately 22 at. %, corresponding to 12%–26% Co/Cu substitution. With respect to Ce content, crystalline  $\text{Ce}_{15.1}\text{Ta}_{1.0}\text{Co}_{74.4}\text{Cu}_{9.5}$  (I) and III contain 15–15.7 at. %, which is lower than the Ce content in  $\text{Ce}_{16.3}\text{Ta}_{0.6}\text{Co}_{68.9}\text{Cu}_{14.2}$  (II) and  $\text{Ce}_{16.3}\text{Ta}_{0.3}\text{Co}_{61.7}\text{Cu}_{21.7}$  (IV) and significantly lower than the approximately 16.7 at. % Ce content required for the exact 1:5 type stoichiometry. Also a minor presence of Ta (0.3–1 at. %) is detected in all five compounds. The Ta content appears to be correlated to the Cu content as seen in Table I. The presence of Ta is explained by the slight dissolution of the inner walls of the Ta reaction container and diffusion of Ta atoms into the liquid at high temperatures. Since no Ta precipitation or segregation is observed in the SEM-EDS analysis of the as-grown crystals, we believe Ta is being incorporated into the crystal structure either as interstices or as uniformly distributed nanoscale precipitates. However, the slight Ce depletion and the presence of Ta suggest the possibility of minor deviations from the classic  $\text{CaCu}_5$ -type crystal structure toward various channel disorders or “dumbbell” problems characterized elsewhere [48–50]. These deviations are accounted for in our structural models and refinements (Figs. 4 and 5).

The SEM backscattered-electron images taken from the (0001) surface of the heat-treated crystals [Figs. 3(a)–3(c), lower panels] show degradation of the single-phase crystal into a bimodal microstructure consisting of a darker matrix

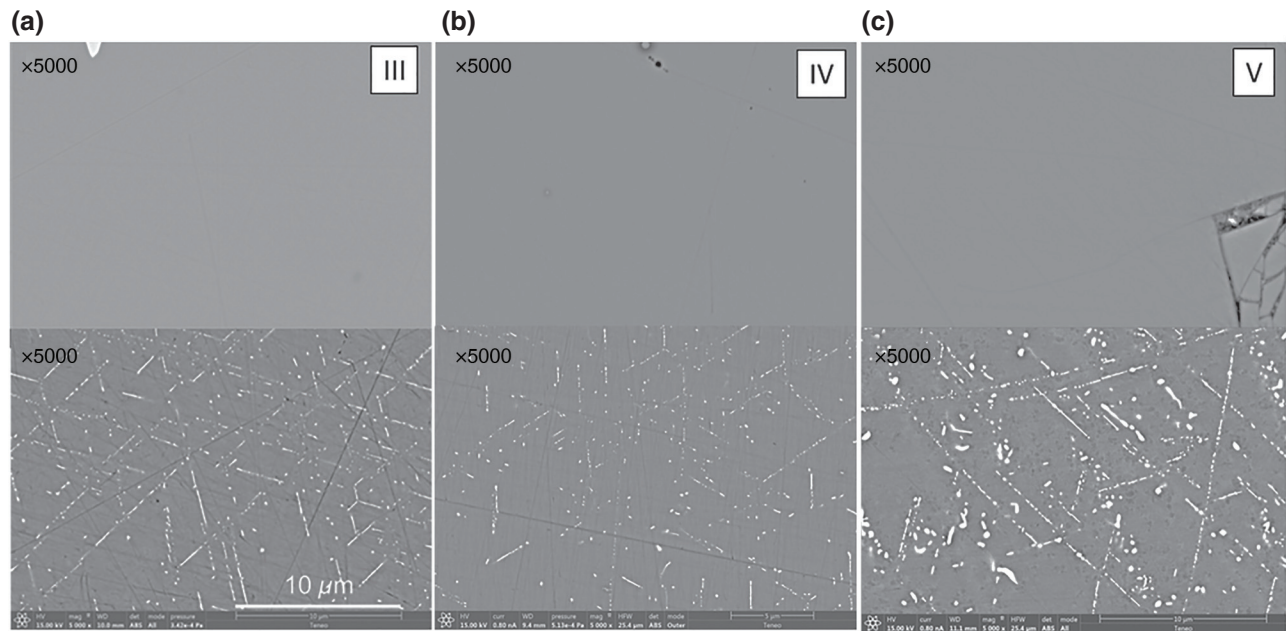


FIG. 3. SEM backscattered-electron images of (a)  $\text{Ce}_{15.7}\text{Ta}_{0.6}\text{Co}_{67.8}\text{Cu}_{15.9}$  (III), (b)  $\text{Ce}_{16.3}\text{Ta}_{0.3}\text{Co}_{61.7}\text{Cu}_{21.7}$  (IV), and (c)  $\text{Ce}_{14.3}\text{Ta}_{1.0}\text{Co}_{62.0}\text{Fe}_{12.3}\text{Cu}_{10.4}$  (V) before (upper panels) and after (lower panels) heat treatment. All images are obtained at a magnification of  $\times 5000$  and 15 kV.

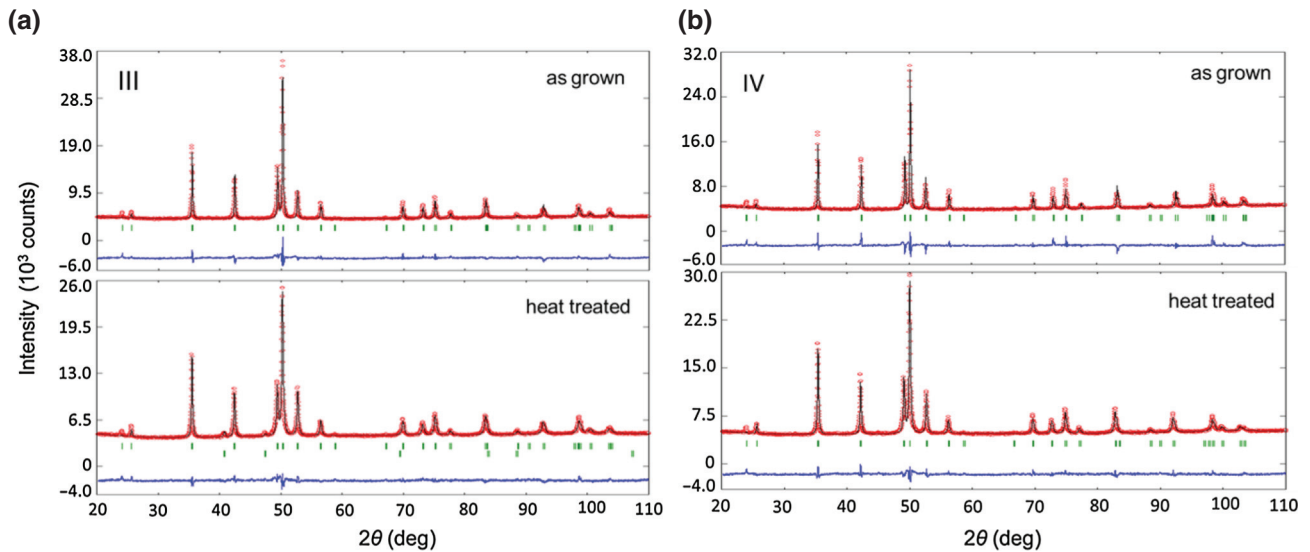


FIG. 4. Powder x-ray patterns and Rietveld refinement results for (a)  $\text{Ce}_{15.7}\text{Ta}_{0.6}\text{Co}_{67.8}\text{Cu}_{15.9}$  (**III**) and (b)  $\text{Ce}_{16.3}\text{Ta}_{0.3}\text{Co}_{61.7}\text{Cu}_{21.7}$  (**IV**) before (upper plots) and after (lower plots) heat treatment. The observed profile is indicated by circles and the calculated profile is indicated by the solid line. Bragg peak positions are indicated by vertical ticks, and the difference is shown at the bottom.

and lighter laminas. These laminas follow the hexagonal symmetry of the original crystal, crossing each other at an angle of  $60^\circ$  or  $120^\circ$ . The thickness of the laminar features is approximately  $0.05$  to  $0.1 \mu\text{m}$ , and their lengths range

from approximately  $1$  to  $10 \mu\text{m}$ . The distances between two laminas are approximately  $2\text{--}3 \mu\text{m}$ . The elemental EDS analysis of the heat-treated material (Table I) indicates the segregation of Ta-rich phases into the laminar

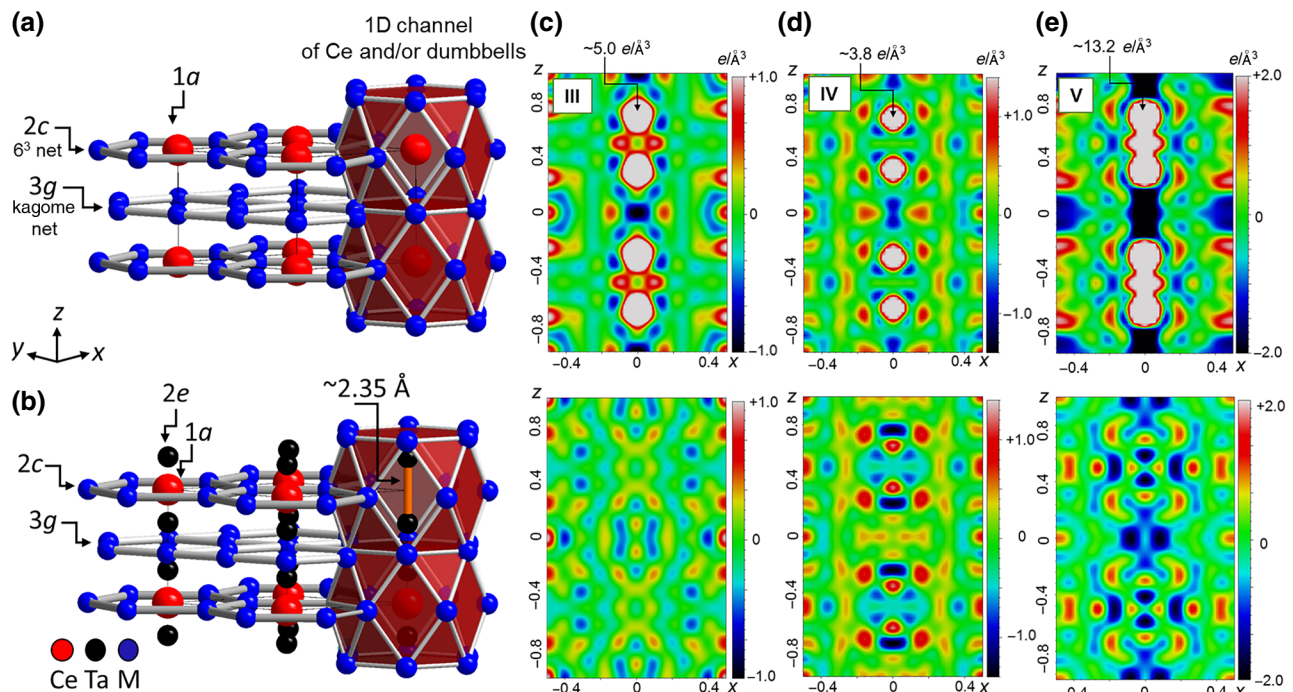


FIG. 5. Single-crystal refinement for  $\text{Ce}_{15.7}\text{Ta}_{0.6}\text{Co}_{67.8}\text{Cu}_{15.9}$  (**III**),  $\text{Ce}_{16.3}\text{Ta}_{0.3}\text{Co}_{61.7}\text{Cu}_{21.7}$  (**IV**), and  $\text{Ce}_{14.3}\text{Ta}_{1.0}\text{Co}_{62.0}\text{Fe}_{12.3}\text{Cu}_{10.4}$  (**V**): [110] views of (a)  $\text{CaCu}_5$ -type and (b)  $\text{TbCu}_7$ -type structures with and without Ta “dumbbells,” respectively, and (c)–(e) difference-electron-density maps of structure solutions without “dumbbells” (upper row) showing significant residual electron density peaks of approximately  $3.5 e/\text{\AA}^3$  to approximately  $13.5 e/\text{\AA}^3$  in 1D structural channels at  $(0\ 0\ z)$ , with  $z \approx 0.3$ , and with “dumbbells” (lower row) with significantly smaller residuals.

features, whereas the matrix material becomes practically Ta-free in the Cu-richest crystal, **IV**.

### B. X-ray analysis and crystal-structure determination

Powder and single-crystal x-ray analyses are performed to determine the structure of crystals of **I**, **II**, **III**, **IV**, and  $\text{Ce}_{14.3}\text{Ta}_{1.0}\text{Co}_{62.0}\text{Fe}_{12.3}\text{Cu}_{10.4}$  (**V**). Rietveld fitting of the powder x-ray pattern taken from the as-grown, crushed, and thoroughly powdered single crystals of **I–V** shows that all Bragg reflections are well indexed within the  $\text{CaCu}_5$ -type structure ( $hP6$ ,  $P6/mmm$ ), providing a strong argument for the single-phase nature of the as-grown crystals in agreement with our SEM observations (Fig. 3). To address the EDS-observed Ta presence and Ce deficiency, especially in the as-grown crystals of **I**, **III**, and **V** (see Table I), we consider known structural derivatives of  $\text{CaCu}_5$  [48]. These derivatives are typically observed in binary and ternary rare earth–transition metal systems near the approximately 1:5 and approximately 2:17 stoichiometries and result from the replacement of rare-earth atoms by pairs of transition-metal atoms. The  $\text{CaCu}_5$  substructure can be retained if the replacement is fully random, as in  $\text{TbCu}_7$  [51], but may be transformed into various superstructures, such as  $\text{Th}_2\text{Zn}_{17}$  [52] and  $\text{Th}_2\text{Ni}_{17}$  [53], if the substitution is ordered. A third possibility comes as a combination of ordered and disordered rare earth–“dumbbell” substitutions that are contained in a superstructure; for example,  $\text{LuFe}_{9.5}$  [54] and  $\text{PrFe}_7$  [55]. We try Rietveld refinements with structural models allowing the presence of Ta but the clear indexing of Bragg reflections within the parent,  $\text{CaCu}_5$ -type, 1:5 structure (Fig. 4) indicates a minor and random distribution of Ta.

We allow Ce/Ta or  $T$ /Ta ( $T = \text{Co}, \text{Cu}, \text{Fe}$ ) statistical mixing on the  $1a$ ,  $2c$ , and  $3g$  sites with and without underoccupancy of Ce on the  $1a$  site. The substitution of Ce atoms by  $T$ - $T$  “dumbbells” is introduced into the model as an independent crystallographic  $2e$  site ( $0\ 0\ z$ ) with  $z \sim 0.3$ . The last model represents a small departure from the  $\text{CaCu}_5$  structure toward the closely related  $\text{TbCu}_7$  structure with slight Ce/“dumbbell” substitution within the one-dimensional hexagonal channel (see Fig. 5). The Ce/Ta and  $T$ /Ta mixings do not produce satisfactory fits, significantly increasing the residuals and showing unreasonable isotropic temperature parameters, whereas the “dumbbell” refinements are insensitive to small amounts of  $T$ - $T$  ( $T = \text{Ta}, \text{Co}, \text{Cu}$ , and/or  $\text{Fe}$ ) pairs and are comparable to those without any Ta and are proportional to the EDS-determined Co/Cu mixings on the  $2c$  and  $3g$  sites, suggesting minimal disorder. Although the present powder x-ray refinements do not clearly address Ta occupation, they clearly determine lattice parameters as well as demonstrate the phase content and purity of the material before and after the heat treatment. Data are presented in Figs. 4(a) and 4(b) (upper panels) for the crushed, as-grown

crystals of **III** and **IV**. Phase analysis of powder x-ray patterns taken from crushed heat-treated crystals of **III** [Figs. 4(a) and 4(b), lower panels] reveals the clear presence of Ta-like impurities [ $Fm\bar{3}m$ ,  $a = 4.446(1)$  Å], confirming the EDS findings (Fig. 3), whereas in **IV** Ta is not detected in the x-ray pattern.

Single-crystal x-ray diffraction of the as-grown crystals shows poor quality of the crystals, suggesting crystal intergrowth, twinning, residual-stress, or stacking-fault effects. These defects are very apparent on Laue frames from numerous (more than ten) specimens of **I** in the form of strong streaking, doubling of the reflections, and sometimes the presence of the Debye rings. However, these effects diminished in **II** and are practically absent in **III** and **IV**, allowing structural characterization of the as-grown crystals of **III–V** (see Table II). Single-crystal structure solutions of **III–V** confirm their  $\text{CaCu}_5$  substructure (see Tables II and III). However, disorder is detected within the 1D hexagonal channels, as seen in the residual-electron-density peaks of approximately  $5.0\ e/\text{Å}^3$ , approximately  $3.8\ e/\text{Å}^3$ , and approximately  $13.2\ e/\text{Å}^3$  at  $(0\ 0\ z)$ ,  $z \approx 0.295$ , for **III**, **IV**, and **V**, respectively. Only by filling the  $2e$  site with the heaviest and largest available pair, Ta-Ta, are we able to reach satisfactory refinement. The  $R_1/wR_2$  residuals dropped by 50%–70% in comparison with the solutions without Ta and showed minimal fluctuations of the residual electron density in the final fits. Figure 5 shows the differential Fourier maps for **III–V** with and without the “dumbbell” disorder. One significant deficiency of the solutions is the interatomic  $T$ - $T$  distance of approximately 2.35 Å, which is typical for Co-Co, Co-Cu, and Co-Fe pairs but is extremely short for the Ta-Ta pair. However, the “dumbbell” configuration with large and heavy atoms similar to Ta is not unprecedented and was reported for the similar structure of  $\text{CeFe}_{10}\text{Zr}_{0.8}$  ( $d_{\text{Zr-Zr}} \approx 2.65$  Å) [56]. However, the stoichiometry of **V** shows significant deviation from the ideal 1:5 stoichiometry. The content of 1D channels (Ce plus the Ta-Ta pairs) does not reach the expected 16.7 at. %, meaning that some of the  $T$  atoms must participate in the channel disorder.

### C. Transmission electron microscopy

Figure 6(a) shows a high-angle-annular-dark-field (HAADF) scanning-transmission-electron-microscope (STEM) image of as-grown **III** showing the overall microstructure. The entire region consists a single-crystal phase. Figure 6(b) shows an enlarged HAADF image that shows a dark-contrast line. It is the only feature that can be found in the entire scan area. Figure 6(c) shows a diffraction pattern taken from the region shown in Fig. 6(b) including the matrix and the dark line. It clearly shows the single-crystal 1:5 phase. It seems that the dark-line region has the same crystal structure and it is not a precipitate, which would have caused additional diffracted

TABLE II. Single-crystal and refinement data for  $\text{Ce}_{15.7}\text{Ta}_{0.6}\text{Co}_{67.8}\text{Cu}_{15.9}$  (**III**),  $\text{Ce}_{16.3}\text{Ta}_{0.3}\text{Co}_{61.7}\text{Cu}_{21.7}$  (**IV**), and  $\text{Ce}_{14.3}\text{Ta}_{1.0}\text{Co}_{62.0}\text{Fe}_{12.3}\text{Cu}_{10.4}$  (**V**). The errors for the lattice parameters are derived from the crystal-structure solution.

	<b>III</b>	<b>IV</b>	<b>V</b>
EDS composition	$\text{Ce}_{0.94}\text{Ta}_{0.04}\text{Co}_{4.06}\text{Cu}_{0.94}$	$\text{Ce}_{0.99}\text{Ta}_{0.00}\text{Co}_{3.70}\text{Cu}_{1.30}$	$\text{Ce}_{0.86}\text{Ta}_{0.06}\text{Co}_{3.72}\text{Fe}_{0.73}\text{Cu}_{0.62}$
Refined composition	$\text{Ce}_{0.98}\text{Ta}_{0.04}\text{Co}_{4.25}\text{Cu}_{0.75}$	$\text{Ce}_{0.99}\text{Ta}_{0.02}\text{Co}_{3.79}\text{Cu}_{1.21}$	$\text{Ce}_{0.94}\text{Ta}_{0.12}\text{Co}_{3.68}\text{Fe}_{0.72}\text{Cu}_{0.60}$
Formula mass (g)	442.68	442.57	449.52
Space group; $Z$	$P6/mmm$ ; 1	$P6/mmm$ ; 1	$P6/mmm$ ; 1
$a$ (Å)	4.946(1)	4.952(1)	4.928(1)
$c$ (Å)	4.038(1)	4.035(1)	4.073(1)
$V$ (Å <sup>3</sup> )	85.57(4)	85.70(5)	85.66(2)
$d_c$ (Mg/m <sup>3</sup> )	8.52	8.57	8.69
Absorption coefficient $\mu$ (mm <sup>-1</sup> ; Mo $K\alpha$ )	37.85	37.08	39.78
Reflections collected/ $R_{\text{int}}$	1631/0.025	2002/0.042	1808/0.027
Independent data/restraints/parameters	79/0/12	109/0/13	91/0/11
Goodness of fit ( $F^2$ )	1.221	1.129	1.172
$R_1/wR_2$ [ $I > 2\sigma(I)$ ]	0.018/0.041	0.021/0.048	0.030/0.063
$R_1/wR_2$ (all data)	0.021/0.041	0.025/0.046	0.031/0.063
Largest diffraction peak/hole ( $e/\text{Å}^3$ )	0.80/ - 0.74	1.04/ - 0.99	1.91/ - 1.53

spots in Fig. 6(c). Figure 6(d) shows a high-resolution STEM image taken from the orange-boxed area in Fig. 6(b) under the  $[\bar{1}10]$  zone axis. The inset shows an enlarged atomic image with an atomic model of the hexagonal 1:5 phase. The bright dots and dark dots in the images correspond to atomic columns of the elements Ce and Co/Cu, respectively. Figure 6(e) shows an enlarged image of the blue-boxed area in Fig. 6(b), and a dark line in the single-crystal phase is shown clearly. Figure 6(f) shows an EDS elemental mapping of Fig. 6(e). The chemical contrast between the matrix and the dark line is observed. The EDS result shows the dark line is Co rich and Cu deficient.

Figure 7(a) shows a HAADF image of an annealed sample showing the overall microstructure. Many bright areas are observed unlike for the unannealed sample shown in Fig. 6. Figure 7(b) shows an enlarged image of the blue-boxed area in Fig. 7(a), and Fig. 7(c) shows the EDS

elemental mapping corresponding to Fig. 7(b). The bright regions in Fig. 7(b) are Ta rich and are considered as Ta precipitates. Additionally, a few dark lines are observed in the Ta precipitate. The difference in the brightness of the precipitates is attributed to the difference in the thickness of each precipitate. Figure 7(d) shows an enlarged image of the orange-boxed area in Fig. 7(b), and Fig. 7(e) shows a diffraction pattern taken from Fig. 7(d) including the matrix and the Ta precipitates. Figure 7(d) shows Ta precipitates coherently embedded by epitaxial precipitation and the corresponding diffraction pattern shows the epitaxial relationship between the matrix and the Ta precipitate. The orientation relation is observed as follows:  $(110) \text{ Ce-Co-Cu} // (110) \text{ Ta}$ ;  $(002) \text{ Ce-Co-Cu} // (\bar{1}10) \text{ Ta}$ ; and  $[\bar{1}10] \text{ Ce-Co-Cu} // [001] \text{ Ta}$ . Figure 7(f) shows a high-resolution STEM image taken from the matrix in Fig. 7(d) under the  $[\bar{1}10]$  zone axis. It is the same as that seen in

TABLE III. Atomic coordinates, equivalent isotropic displacement parameters ( $10^3 \text{ \AA}^2$ ), and site-occupancy factors (SOF) refined for  $\text{Ce}_{15.7}\text{Ta}_{0.6}\text{Co}_{67.8}\text{Cu}_{15.9}$  (**III**),  $\text{Ce}_{16.3}\text{Ta}_{0.3}\text{Co}_{61.7}\text{Cu}_{21.7}$  (**IV**), and  $\text{Ce}_{14.3}\text{Ta}_{1.0}\text{Co}_{62.0}\text{Fe}_{12.3}\text{Cu}_{10.4}$  (**V**).

Atom	Wyckoff position	$x$	$y$	$z$	$U_{\text{eq}}$	SOF	Compound
Ce	$1a$	0	0	0	15(1)	0.977(2)	III
					16(1)	0.988(1)	IV
					19(1)	0.936(3)	V
Ta	$2e$	0	0	0.280(6)	15(1)	0.023(2)	III
				0.296(9)	16(1)	0.012(1)	IV
				0.292(4)	19(1)	0.064(3)	V
$M1^a$	$2c$	2/3	1/3	0	14(1)	1.00 Co	III
					15(1)	0.23(7) Cu	IV
					23(1)	1.00 Co	V
$M2^a$	$3g$	1/2	0	1/2	10(1)	0.25(6) Cu	III
					10(1)	0.25(5) Cu	IV
					10(1)	0.24 Fe/0.20 Cu	V

<sup>a</sup>The letter  $M$  stands for Co/Cu or Co/Fe/Cu mixed occupancy;  $3g$  occupancy for **V** is fixed.

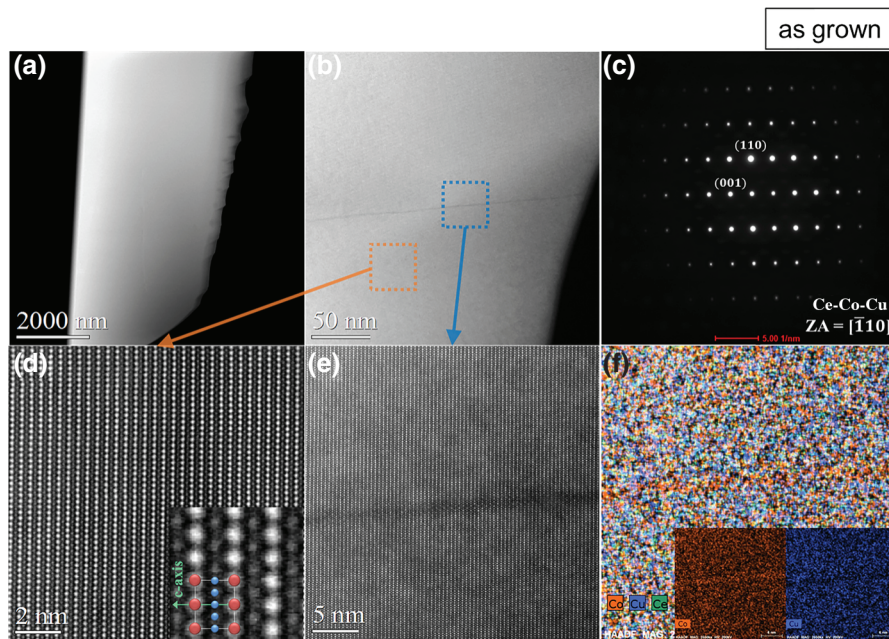


FIG. 6. (a) HAADF STEM image of as-grown  $\text{Ce}_{15.7}\text{Ta}_{0.6}\text{Co}_{67.8}\text{Cu}_{15.9}$  (**III**) showing the overall microstructure. (b) Enlarged HAADF image showing a dark-contrast line. (c) Diffraction pattern taken from the region shown in (b) including the matrix and the dark line. (d) High-resolution STEM image taken from the orange-boxed area in (b) under the  $[\bar{1}10]$  zone axis (ZA). The inset is an enlarged atomic image with an atomic model of the hexagonal 1:5 Ce/Co/Cu phase. The bright dots and dark dots in the images correspond to atomic columns of the elements Ce, and Co and Cu, respectively. (e) Enlarged image of the blue-boxed area in (b); the dark line in the single-crystal phase is shown clearly. (f) EDS elemental mapping of (e) clearly showing Co enrichment in the line; the small Co and Cu elemental maps in the insets are presented to contrast observation of Cu depletion in the same line.

Fig. 6(d). The inset shows an enlarged atomic image with an atomic model of the hexagonal 1:5 Ce/Co/Cu phase. The bright dots and dark dots in the images correspond to atomic columns of the elements Ce and Co/Cu, respectively. Figure 8 shows high-resolution HAADF images of

the interface between the matrix and the Ta precipitate taken from red-boxed area in Fig. 7(d) and the corresponding EDS-elemental-mapping results [Figs. 7(b)–7(f)]. The dashed white lines indicate the same position in each image. Although a Cu-rich and Co-deficient region is

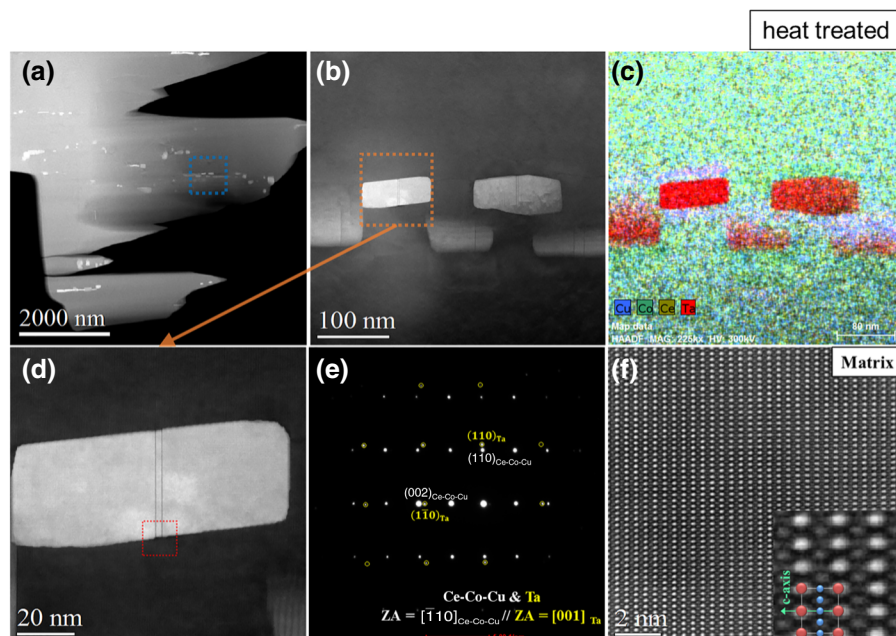


FIG. 7. (a) HAADF image of heat-treated  $\text{Ce}_{15.7}\text{Ta}_{0.6}\text{Co}_{67.8}\text{Cu}_{15.9}$  (**III**) showing the overall microstructure. (b) Enlarged image of the blue-boxed area in (a). (c) EDS elemental mapping corresponding to (b). The bright regions are Ta rich and considered as Ta precipitate. (d) Enlarged image of the orange-boxed area in (b). (e) Diffraction pattern taken from (d) including the matrix and the Ta precipitate. (f) High-resolution STEM image obtained from the matrix in (d) under the  $[\bar{1}10]$  zone axis (ZA).



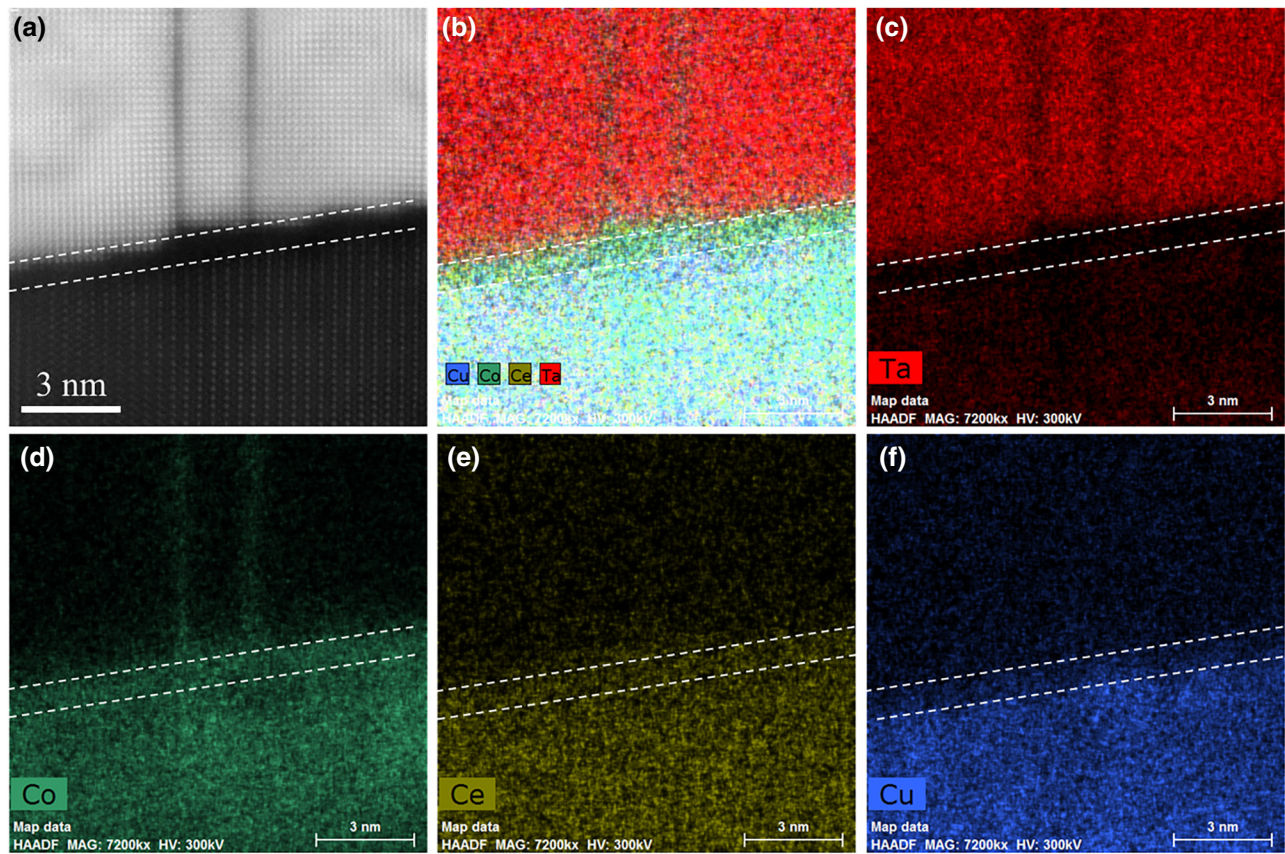


FIG. 8. (a) High-resolution HAADF image of the interface between the matrix and the Ta precipitate taken from the red-boxed area in Fig. 7(d). (b)–(f) Corresponding EDS-elemental-mapping results. The white lines indicate the same position in each image.

observed near the precipitate [Fig. 7(c)], there is also a Co-rich, Ce-rich, and Cu-deficient interface between the matrix and the Ta precipitate. The dark lines in the Ta precipitate are Co rich. From the EDS maps at the interface and near the precipitate, it is assumed that Co infiltrated into the precipitate [Fig. 7(d)], and Co became deficient near the precipitate with relative Co richness as a result. As discussed below, the high-resolution-TEM results for both as-grown and heat-treated samples of crystalline III will be used to elucidate the pinning mechanism that leads to significant coercivities in the crystals.

#### IV. MAGNETIC PROPERTIES

##### A. As-grown crystals: Curie temperature, magnetocrystalline anisotropy field, and energy density

Figure 9 presents the Curie temperatures for I–V as inferred from the peak in  $dM/dT$  shown in the inset. The Curie temperatures  $T_C$  estimated from the minimum in the derivative correspond closely to the Curie temperatures derived via the more-accurate Arrot-plot method (see below).  $T_C$  decreases rapidly with increasing Cu content for Fe-free I–IV. This is consistent with an early

report [36] and indicates weakening in the ferromagnetic exchange interactions within the Co sublattice due to the introduction of nonmagnetic Cu. In contrast, the crystal of Fe-doped V shows a remarkable increase of  $T_C$ , increasing

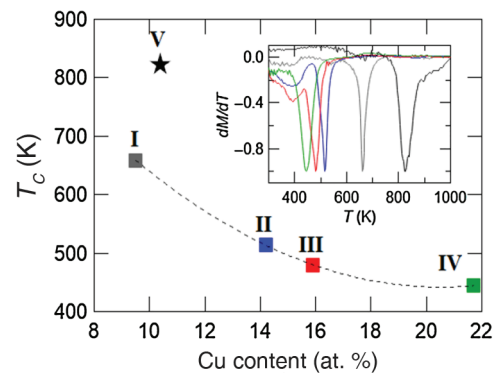


FIG. 9. Curie temperatures for as-grown  $\text{Ce}_{15.1}\text{Ta}_{1.0}\text{Co}_{74.4}\text{Cu}_{9.5}$  (I),  $\text{Ce}_{16.3}\text{Ta}_{0.6}\text{Co}_{68.9}\text{Cu}_{14.2}$  (II),  $\text{Ce}_{15.7}\text{Ta}_{0.6}\text{Co}_{67.8}\text{Cu}_{15.9}$  (III),  $\text{Ce}_{16.3}\text{Ta}_{0.3}\text{Co}_{61.7}\text{Cu}_{21.7}$  (IV), and  $\text{Ce}_{14.3}\text{Ta}_{1.0}\text{Co}_{62.0}\text{Fe}_{12.3}\text{Cu}_{10.4}$  (V) inferred from the peaks in the derivative of magnetization with respect to temperature (i.e.,  $dM/dT$ ) obtained for each crystal (see the inset). Magnetization data are obtained under a magnetic field of 0.01 T.

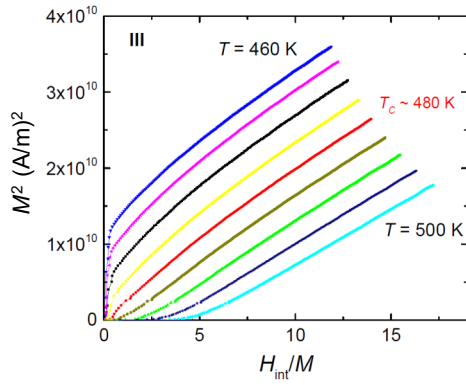


FIG. 10. Arrott plot for  $\text{Ce}_{15.7}\text{Ta}_{0.6}\text{Co}_{67.8}\text{Cu}_{15.9}$  (**III**) with isotherms taken at 5.0-K intervals as indicated. The Curie temperature is approximately 480 K as inferred from the plot since the isotherm is closest to linear and passes through the origin.

by more than 150 K to approximately 820 K, a value that is significantly higher than the Curie temperature (653 K) of the parent  $\text{CeCo}_5$  [57]. Using band-structure analysis, we find that Fe doping of  $\text{CeCo}_5$  and  $\text{Ce}(\text{Co}, \text{Cu})_5$  increases the ordering energy  $\Delta E = E_{\text{nonmagnetic}} - E_{\text{ferromagnetic}}$  as well as the total magnetic moment of the systems (see Sec. V). This leads to the remarkable increase of the Curie temperature and saturation magnetization.

To more formally determine  $T_C$ , we perform an Arrott-plot analysis for **III** using isotherms between 460 to 500 K (Fig. 10). The Curie temperature for **III** is estimated to be approximately 480 K since the isotherm at that temperature is closest to a straight line and passes through the origin. In Fig. 11 we show representative  $M(H)$  isotherms for **V**. In

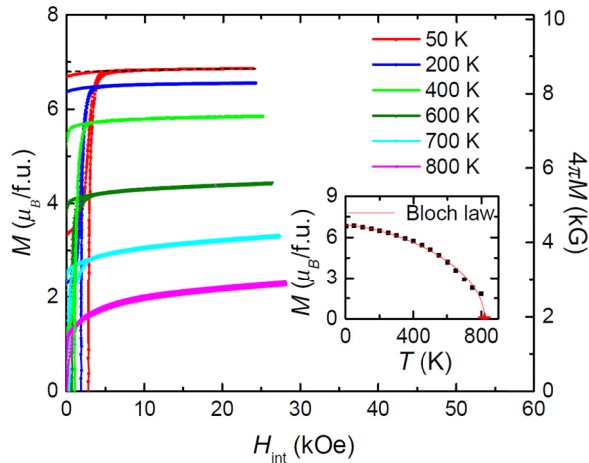


FIG. 11. Representative  $M(H)$  isotherms for the as-grown crystal of  $\text{Ce}_{14.3}\text{Ta}_{1.0}\text{Co}_{62.0}\text{Fe}_{12.3}\text{Cu}_{10.4}$  (**V**). The inset shows spontaneous magnetization for each temperature inferred from the extrapolation of the linear regions of  $M(H)$  back to  $H = 0$ . The red star shows the extrapolated  $T_C$  following Bloch's law:  $M(T) = M(0)[1 - (T/T_C)^{3/2}]$ . f.u., formula unit.

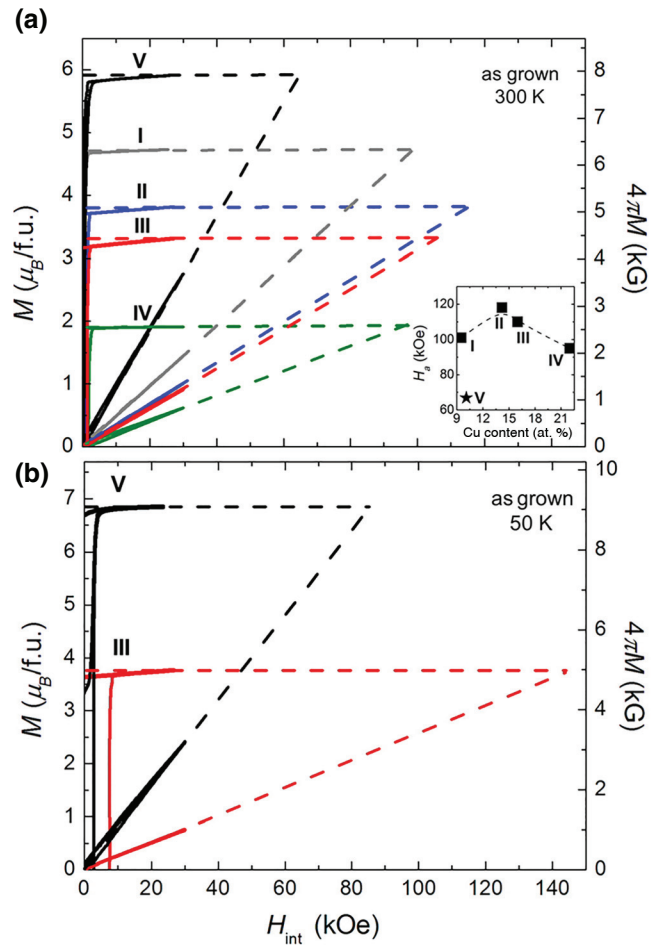


FIG. 12. (a) Anisotropic field-dependent magnetization along the easy and hard axes of as-grown crystals of  $\text{Ce}_{15.1}\text{Ta}_{1.0}\text{Co}_{74.4}\text{Cu}_{9.5}$  (**I**),  $\text{Ce}_{16.3}\text{Ta}_{0.6}\text{Co}_{68.9}\text{Cu}_{14.2}$  (**II**),  $\text{Ce}_{15.7}\text{Ta}_{0.6}\text{Co}_{67.8}\text{Cu}_{15.9}$  (**III**),  $\text{Ce}_{16.3}\text{Ta}_{0.3}\text{Co}_{61.7}\text{Cu}_{21.7}$  (**IV**), and  $\text{Ce}_{14.3}\text{Ta}_{1.0}\text{Co}_{62.0}\text{Fe}_{12.3}\text{Cu}_{10.4}$  (**V**) at 300 K. The inset shows the dependence of the anisotropy field  $H_a$  on Cu concentration, (b) Anisotropic field-dependent magnetization along the easy and hard axes of as-grown crystals of  $\text{Ce}_{15.7}\text{Ta}_{0.6}\text{Co}_{67.8}\text{Cu}_{15.9}$  (**III**) and  $\text{Ce}_{14.3}\text{Ta}_{1.0}\text{Co}_{62.0}\text{Fe}_{12.3}\text{Cu}_{10.4}$  (**V**) at 50 K. f.u., formula unit.

the inset we plot the spontaneous magnetization for each temperature inferred from the extrapolation of the linear region of  $M(H)$  back to  $H = 0$ . As can be seen, these data suggest  $T_C \sim 820$  K (estimated by generalized Bloch-law fitting of spontaneous magnetization), in good agreement with Fig. 9.

Figure 12(a) shows the magnetocrystalline anisotropy field,  $H_a$ , at room temperature for as-grown crystals of **I–V**; the low-temperature estimations of  $H_a$  are done for crystals of **III** and **V** and are presented in Fig. 12(b). The anisotropy field is estimated by the high-field, linear extrapolation of the field-dependent moment along the easy [001] and hard ( $H \perp [001]$ ) axes [22,47]. The room-temperature  $H_a$  for the Fe-free, as-grown crystals of **I–IV**

exhibits a maximum anisotropy field of approximately 118 kOe in crystalline **II**. The addition of Fe has a detrimental influence on the magnetocrystalline anisotropy (in Fe-doped **V** the anisotropy field drops to approximately 65 kOe [see the inset in Fig. 12(a)], but the spontaneous magnetization increases by approximately 30% compared with crystals with similar Cu contents). Low-temperature measurements estimate the spontaneous magnetization for crystals of **III** and **V** to be approximately  $3.7 \mu_B$  per formula unit and approximately  $6.8 \mu_B$  per formula unit, respectively.

The temperature-dependent magnetocrystalline anisotropy energy density is measured by the Sucksmith-Thompson method [47,58,59] by use of the hard-axis magnetization isotherms for crystals of **III** and **V** (Fig. 13). In this method, the  $y$  intercept ( $I$ ) of the  $H_{\text{int}}/M_{\perp}$ -versus- $M_{\perp}^2$  curve is used to determine  $K_1$  as  $I = 2K_1/M_S^2$ , where  $M_{\perp}$  is the hard-axis magnetization and  $M_S$  is the saturation magnetization. The corresponding uncertainty in measurement is determined with the formula  $\Delta K_1 = K_1(\Delta I/I + 2\Delta M_S/M_S)$  [60]. The uncertainty  $\Delta I$  is determined from the uncertainty of the linear fit.  $\Delta M_S$  is determined from the difference between the maximum possible upper bound of the saturation magnetization [obtained as the  $y$  intercept of  $M$  versus  $1/H$ ] and lower bound of the saturation magnetization [obtained as the linear fit of  $M(H)$  data as shown in the 50-K magnetization data in Fig. 11] for each temperature.

The as-grown single crystals show magnetic hysteresis when measured along the easy axis of magnetization [001]. For example, crystalline **III** exhibited a hysteresis (see Fig. 1) that reached  $H_c \approx 1.6$  kOe and  $B_r \approx 4.2$  kG,  $M_s \approx 4.2$  kG, and  $(BH)_{\text{max}} \approx 3.5$  MGOe (Fig. 14), which is comparable to most of anisotropic sintered alnico

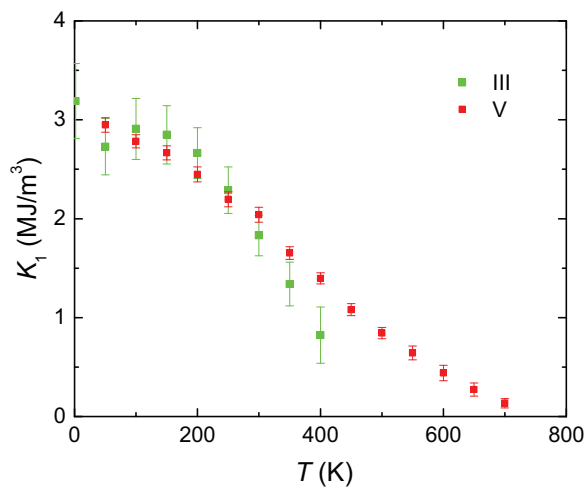


FIG. 13. Comparison of temperature-dependent magnetocrystalline anisotropy energy density of  $\text{Ce}_{15.7}\text{Ta}_{0.6}\text{Co}_{67.8}\text{Cu}_{15.9}$  (**III**) and  $\text{Ce}_{14.3}\text{Ta}_{1.0}\text{Co}_{62.0}\text{Fe}_{12.3}\text{Cu}_{10.4}$  (**V**).

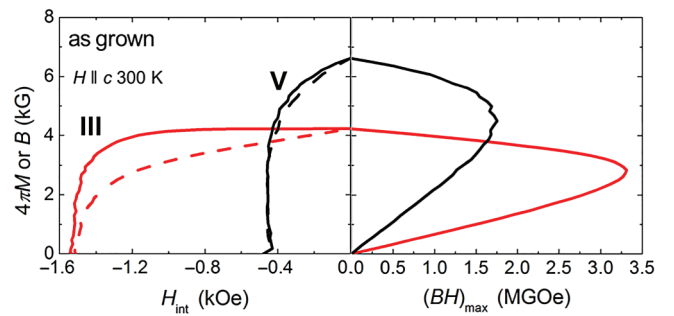


FIG. 14. Room-temperature second-quadrant magnetic hysteresis loops for as-grown crystals of  $\text{Ce}_{15.7}\text{Ta}_{0.6}\text{Co}_{67.8}\text{Cu}_{15.9}$  (**III**) and  $\text{Ce}_{14.3}\text{Ta}_{1.0}\text{Co}_{62.0}\text{Fe}_{12.3}\text{Cu}_{10.4}$  (**V**).  $4\pi M$  is indicated by the solid line and  $B$  is indicated by the dashed line in the left panel. Estimation of the energy products  $(BH)_{\text{max}}$  (right panel).

grades [61]. This is remarkable considering the common belief that the appearance of the coercivity is a result of the extrinsic properties (e.g., development of proper microstructure for strong magnetic domain pinning), and this is generally not associated with a single-phase single crystal as determined by the SEM and XRD examinations (Figs. 3 and 4), which did not reveal any elemental precipitations, segregations, or microstructure on their corresponding length scales.

The detailed high-resolution STEM examination of as-grown **III** (Fig. 6) shows the basic uniformity and integrity with small Co-enriched and Cu-depleted regions/stripes coherently dispersed throughout the matrix. Unfortunately, the size of these stripes does not allow EDS composition determination or structural analysis. However, on the basis of previous reports [21–23], we assume that these are embryonic structural defects caused by stacking faults compensating for various channel disorders within the material. They may also be the nucleation sites for the decomposition and/or miscibility gap as suggested in previous literature [36].

## B. Heat-treated crystals: coercivity, pinning, and magnetic energy

After heat treatment, crystals of **I–IV** show significantly increased magnetic hysteresis with a monotonic increase of coercivity,  $H_c$ , and a linear decrease of spontaneous magnetization,  $M_s$ , with increasing Cu content (Fig. 15). For example, the magnetic characteristics of **III** change as follows: significant increase of  $H_c$  from approximately 1.6 kOe to approximately 6.3 kOe with an increase of  $B_r$  ( $M_s$ ) from approximately 4.2 (4.2) kG to approximately 5.3 (5.7) kG, resulting in  $(BH)_{\text{max}}$  of approximately 7.8 MGOe [Fig. 16]. In addition to the conspicuous increase in magnetic hysteresis, there is a noteworthy increase in saturation magnetization of the heat-treated samples (Fig. 1 and upper inset in Fig. 15). These increases in magnetic hysteresis and saturation magnetization correlate with the

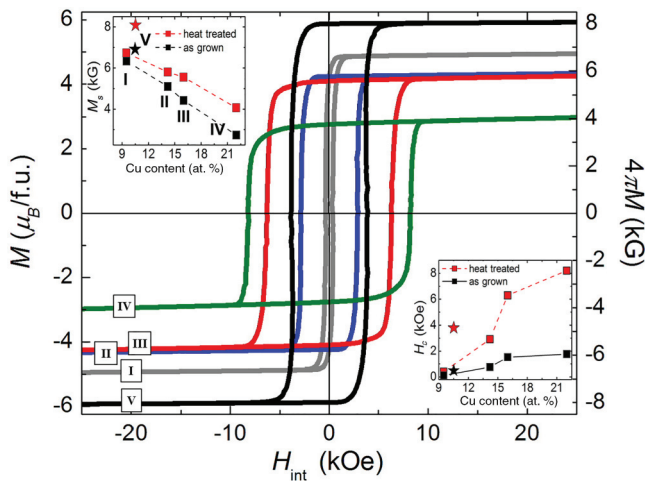


FIG. 15. Magnetic hysteresis loops of heat-treated crystals of  $\text{Ce}_{15.1}\text{Ta}_{1.0}\text{Co}_{74.4}\text{Cu}_{9.5}$  (I),  $\text{Ce}_{16.3}\text{Ta}_{0.6}\text{Co}_{68.9}\text{Cu}_{14.2}$  (II),  $\text{Ce}_{15.7}\text{Ta}_{0.6}\text{Co}_{67.8}\text{Cu}_{15.9}$  (III),  $\text{Ce}_{16.3}\text{Ta}_{0.3}\text{Co}_{61.7}\text{Cu}_{21.7}$  (IV), and  $\text{Ce}_{14.3}\text{Ta}_{1.0}\text{Co}_{62.0}\text{Fe}_{12.3}\text{Cu}_{10.4}$  (V) at 300 K. The upper-right inset shows the dependence of the spontaneous magnetization  $M_s$  on Cu concentration for the as-grown and heat-treated crystals. The lower-right inset shows the dependence of the coercivity  $H_c$  on Cu concentration for the as-grown and heat-treated crystals. f.u., formula unit.

appearance of the Ta-rich precipitates (see SEM images in Fig. 3). The STEM analysis confirms that these are 90%–95%-pure rectangular blocks of Ta (according to the diffraction patterns and elemental analysis) and their interfaces are coherent with the matrix material. However, high-magnification TEM EDS maps [Figs. 7(c) and 8] reveal a Cu-deficient and Co-enriched layer at the interface of the precipitates and the matrix, and Co is detected in precipitates as lines, which somewhat resemble observations of rare Co-enriched and Cu-depleted lines in the STEM examination of as-grown crystals (Fig. 6). These results suggest that the high coercivity may be explained by the Ta-rich precipitates serving as pinning sites and

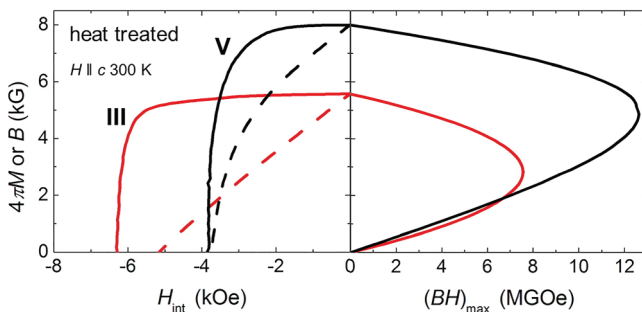


FIG. 16. Room-temperature second-quadrant magnetic hysteresis loops for heat-treated crystals of  $\text{Ce}_{15.7}\text{Ta}_{0.6}\text{Co}_{67.8}\text{Cu}_{15.9}$  (III) and  $\text{Ce}_{14.3}\text{Ta}_{1.0}\text{Co}_{62.0}\text{Fe}_{12.3}\text{Cu}_{10.4}$  (V).  $4\pi M$  is indicated by the solid line and  $B$  is indicated by the dashed line in the left panel. Estimation of the energy products  $(BH)_{\max}$  (right panel).

can be described with a simple domain-pinning model. Typically, the coercive force is inversely proportional to the saturation magnetization for a particular magnetocrystalline energy ( $H_c = \sqrt{AK}/M_s l$ , where  $A$  is the exchange constant,  $K$  is the magnetocrystalline anisotropy,  $M_s$  is the saturation magnetization, and  $l$  is the distance between the precipitates) [21–23]. According to the equation, by increasing the amount of pinning precipitates, we decrease the volume fraction of the matrix material and magnetization  $M_s$  of the system. Also, the distances  $l$  between the precipitates become shorter. As a result, the coercivity  $H_c$  increases. Thus,  $H_c$  of our crystals should be directly proportional to the Ta content. However, we observe the inverse proportionality: the total Ta content monotonically decreases in crystals of I–IV (Table I), whereas the coercivity monotonically increases (Fig. 15).

In contrast, the  $H_c$  increase correlates directly with increasing Cu content (Fig. 15, see both insets), also following the proposed precipitation coercivity mechanism (see the equation above). Pinning of magnetic domains should occur on the precipitates, the amount of which is regulated by Cu content rather than Ta content. However, we do not observe precipitates that are clearly associated with Cu, except for Ta-depleted regions observed in STEM experiments [Figs. 7(c) and 8].

Therefore, we consider the Ta-rich precipitates as a secondary effect, which decorates the extended three-dimensional (3D) defects and structural imperfections that originate from Cu-depleted and Co-enriched lines observed in the as-grown crystals (Fig. 6) and consequently develop into the regions between Ta-rich precipitates and the matrix in the thermally aged crystals [Figs. 7(c) and 8]. The amount of these imperfections must increase with increasing Cu content and lead to increased coercivity.

According to the literature, coercivity in Cu- and Fe-substituted  $\text{CeCo}_5$  is caused by fine precipitates that originate from partial matrix decomposition similar to eutectoid decomposition observed in pure  $\text{CeCo}_5$  [21–23], whereas in Cu-substituted  $\text{CeCo}_5$  the pronounced coercivity is related to a miscibility gap with a critical temperature close to 800 °C [36]. Both observations support the idea of intragranular domain pinning on extended 3D defects created as a result of matrix phase transformations during the heat treatment (hardening) of the samples. In the first case, the precipitated 2:17 phase, being more anisotropic than the matrix, serves as a pinning site and contributes slightly to the increase in magnetization. In the second case, because of decreased miscibility at lower temperatures, two phases with similar Cu:Co ratios and different Curie temperatures exist. The Cu-poor phase supposedly serves as a pinning precipitate with increased magnetization, and the Cu-richer phase contributes to the higher-anisotropy matrix. One indirect confirmation of such a mechanism is observed in the Fe-free crystals of I–IV, which show atypical and

increasing magnetization after the heat treatment (see the left inset in Fig. 15). This suggests a change of the magnetic nature of the matrix. However, this must occur with a minimal composition change as no significant difference in compositions is detected before and after the heat treatment (Table I). With the addition of Fe, the decomposition process becomes complicated, and besides the miscibility gap, the precipitation of the very stable 2:17 Ce-Cu-Fe phase is possible [21–23]. This, however, is not clearly confirmed in the Fe-doped crystal of **V**. Current SEM-EDS examinations of **V** show a microstructure similar to that of the Fe-free crystals of **III** and **IV** (Fig. 3). After the heat treatment, the 2:17 phase is not observed.

Another explanation for the pronounced increase in magnetization after the heat treatment may be associated with removal of Ta from the matrix material. The increase in magnetization is most pronounced in **IV** with the greatest removal of Ta after the heat treatment (see Table I). One possible explanation for the surprisingly large impact of the removal of Ta on the magnetic properties of our CeCo<sub>5</sub>-based material is as follows. Previous theoretical work [62] found that CeCo<sub>5</sub> is surprisingly near to a nonmagnetic state, on the basis of Stoner physics, despite its substantial Curie point. We suggest that Ta may locally drive the system toward a nonmagnetic or less-magnetic state, so its removal may restore or enhance magnetic character locally. Further theoretical work is clearly needed to address this notion, and it may well be difficult to account quantitatively for the observed magnitude of the behavior—approximately 25% increase in magnetization for the removal of 0.3 at. % Ta. Nevertheless, systems near a magnetic instability can exhibit a disproportionate response to small impurity concentrations, as in paramagnetic Fe impurities having huge effective moments in a Pd-Rh matrix [63], and we suggest the possibility of similar behavior here.

## V. THEORETICAL CALCULATIONS

There are two main questions associated with the extraordinary magnetic nature of Cu- and Fe-substituted CeCo<sub>5</sub>: (i) strong increase of both the Curie temperature and the magnetization caused by the addition of Fe and (ii) the high coercivity that is driven primarily by a Cu-regulated intragranular pinning mechanism rather than the more-typical strong magnetocrystalline anisotropy. We address these in the following subsections through theoretical calculations and multiscale modeling.

### A. Increase of Curie temperature in Fe-doped samples

To understand the observed magnetic behavior and increase in the Curie point with Fe substitution, first-principles calculations for CeCo<sub>5</sub> and CeCo<sub>4</sub>Cu are performed with the density-functional theory as implemented in the WIEN2K code [64]. Calculations are performed

with the experimental lattice parameters. In this structure all internal coordinates are symmetry dictated, so no internal-coordinate optimization is performed. The linear-augmented-plane-wave (LAPW) sphere radii are set to 2.4 bohr for Ce and 2.0 bohr for Co and Cu. In addition, to ensure proper convergence of the basis set,  $Rk_{\max} = 9.0$  is used. Here  $R$  and  $k_{\max}$  are the smallest LAPW sphere radius and the largest interstitial plane-wave cut-off, respectively. All the calculations are performed by our assuming a collinear spin arrangement. The magnetic anisotropy energy (MAE) is obtained by our calculating the total energies of the system with spin-orbit coupling as  $K = E_{[100]} - E_{[001]}$ , where  $E_{[110]}$  and  $E_{[001]}$  are the total energies for the magnetization oriented along the  $a$  and  $c$  directions, respectively. For these MAE calculations the convergence with respect to the number of  $K$  points is carefully checked. All the MAE results reported in this section correspond to 2000  $K$  points in the full Brillouin zone. To correctly treat the strong interactions between the Ce  $f$  electrons, the Hubbard  $U$  correction is applied, with  $U_{\text{Ce}} = 3.0$  eV. For the DFT-with-the-Hubbard- $U$ -parameter (DFT+ $U$ ) calculations, the standard self-interaction-correction [65,66] method is used.

For the modeling of CeCo<sub>4</sub>Cu, Cu is substituted in the Co hexagonal ring ( $2c$  Co site), as our calculations find this location for Cu to be energetically favorable (relative to the  $3g$  site) by some 30 meV/Cu. Fe alloying in CeCo<sub>4</sub>Cu is realized within the virtual-crystal approximation. The calculated magnetic behavior for CeCo<sub>5</sub> is in good agreement with the experimental measurements with a total magnetization of  $6.8 \mu_B$  per unit cell. The calculated spin moment on each  $2c$  Co atom is  $1.42 \mu_B$ , whereas the moment on  $3g$  Co atoms is  $1.5 \mu_B$ . This is accompanied by an orbital moment of approximately  $0.13 \mu_B$ . The calculated Cr spin moment is  $-0.71 \mu_B$ . On Cu substitution (for CeCo<sub>4</sub>Cu) the moment on the Co atoms is reduced to  $1.18 \mu_B$  on the  $2c$  Co site and to  $1.40 \mu_B$  on the  $3g$  Co site. However, on Fe alloying in CeCo<sub>4</sub>Cu (CeCo<sub>4-x</sub>Fe<sub>x</sub>Cu), the total magnetization in the unit cell increases linearly with Fe doping as shown in Fig. 17(a). The calculated MAE of approximately  $3.17 \text{ MJ/m}^3$  without inclusion of the Hubbard  $U$  parameter ( $U = 0$ ) is rather small when compared with the experimental MAE of  $10.5 \text{ MJ/m}^3$  [57]. However a generalized-gradient-approximation-with-the-Hubbard- $U$ -parameter calculation with  $U_{\text{Ce}}$  of 3.0 eV gives a MAE of approximately  $9.0 \text{ MJ/m}^3$ , in good agreement with the experimental value.

The most-remarkable observation of experimental measurements is the increase in the Curie temperature of CeCo<sub>5</sub> when it is alloyed with Cu and Fe. We explain this observation using two methods, one more roughly qualitative, the other more quantitative. For the first method, we note that for a local-moment magnetic material, the Curie point is ultimately controlled by the interatomic exchange interactions, which are often determined by an effective

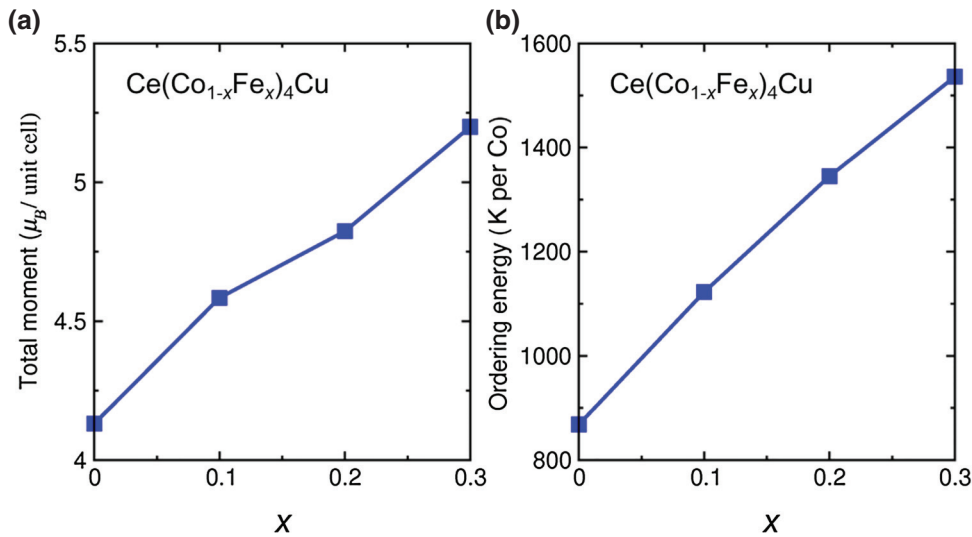


FIG. 17. Total moment as a function of Fe doping (left) and the energy difference between the nonmagnetic state and the ground state (ferromagnetic state) in Kelvins on a per-Co/Fe basis as a function of Fe doping for  $\text{Ce}(\text{Co}_{1-x}\text{Fe}_x)_4\text{Cu}$  (right).

mapping of the first-principles-calculated energies of various magnetic configurations to a Heisenberg-type model. However, the magnetic configurations considered here (with use of the parameters above) all converge instead to the spin-polarized case with all Co spins aligned in the ferromagnetic fashion. These calculations suggest that the magnetism in this material is of itinerant type.

For such a system the calculation of the Curie point is more involved. For this first qualitative approach we therefore limit ourselves to a simple consideration of the magnetic ordering or formation energy—the energy difference  $\Delta E = E_{\text{NM}} - E_{\text{FM}}$ , where  $E_{\text{NM}}$  is the energy of a nonmagnetic configuration and  $E_{\text{FM}}$  is the energy of the ferromagnetic configuration. While this energy contains contributions from both the *intra-atomic* Hund-rule coupling (which does not determine Curie points) and the *interatomic* exchange coupling (which does determine Curie points), it is plausible that within a given alloy system, such as  $\text{CeCo}_{4-x}\text{Fe}_x\text{Cu}$ , the *trend* of the Curie point with alloying is generally captured by the *trend* of this energy. For example, the general quenching of  $3d$ -orbital moments in magnetic systems away from the atomic limit indicates, as expected, that the atomic Hund-rule coupling is not the only relevant interaction here.

To get some insight into the Curie temperature, we therefore calculate this energy  $\Delta E$  for  $\text{Ce}(\text{Co}_{1-x}\text{Fe}_x)_4\text{Cu}$  on a per Co/Fe basis. This, along with the associated magnetic moment, is plotted in Fig. 17 as a function of Fe doping. One observes a substantial ordering-energy increase (from approximately 900 K to approximately 1500 K) with increasing Fe doping from  $x = 0$  to 0.3, along with a substantial magnetic moment increase. From a theoretical standpoint, it is noteworthy that  $\Delta E$  is as high as 1500 K for  $x = 0.3$ . This large energy suggests the possibility of some local character of the magnetism on the  $3d$  (i.e., Co and Fe) atoms with increased Fe content in  $\text{Ce}(\text{Co}_{1-x}\text{Fe}_x)_4\text{Cu}$ . A previous theoretical treatment

of  $\text{CeCo}_5$  [67] found evidence, as we do here, for itinerant character in  $\text{CeCo}_5$ , so the increased Fe contents in these materials are of both theoretical and experimental interest.

Our second method of calculating the Curie point of this system is more quantitative. While the increase of magnetization and the corresponding magnetic formation energy (Fig. 17) with the addition of Fe atoms to  $\text{CeCo}_5$  is generally expected, the observed increase of the Curie temperature  $T_C$  requires a more-detailed explanation. To describe theoretically the dependence of  $T_C$  on the concentration of Fe, we use the traditional mean-field approximation for systems with nonequivalent magnetic atoms in a primitive cell. In this approximation  $T_C$  of a system with  $N$  nonequivalent magnetic atoms is calculated as the largest solution of the equation

$$\det(T_{nm} - T\delta_{nm}) = 0, \quad (1)$$

where  $n$  and  $m$  are the indices of the nonequivalent magnetic sublattices and  $T_{nm} = (2/3)J_{mn}^0$ , where  $J_{mn}^0$  is an effective magnetic exchange interaction of an atom from sublattice  $n$  with all other atoms from the sublattice  $m$ . The exchange-coupling parameters  $J_{mn}^0$  are obtained with the multiple-scattering-formalism expression obtained in Ref. [68] and extensively tested in Ref. [69]. The corresponding dependence on content is described with use of the coherent-potential approximation (see details in Ref. [70]).

The calculations for pure  $\text{CeCo}_5$  reveal that  $T_C$  is determined by the strong ferromagnetic nature of the Co-Co interactions. The absolute value of the exchange parameters decays quickly with increasing interatomic distance, so the main contribution to  $T_C$  comes from the interaction between atoms lying within the distance of the two first neighboring shells. The average value of the nearest-neighbor coupling  $J_{\text{Co-Co}}$  is approximately 15 meV. The contribution from Ce atoms is weak and negative.

The obtained MFA value of  $T_C = 790$  K in  $\text{CeCo}_5$  shows the typical overestimation of the experimental  $T_C$  in this classical spin approach. The addition of Fe atoms shows an interesting development of exchange coupling. First, we notice the appearance of a strong ferromagnetic Fe-Co coupling,  $J_{\text{Fe-Co}} = 21$  meV. Second, the addition of Fe atoms increases the magnetic moments on Co atoms by approximately  $0.1 \mu_B$ , with a corresponding increase of Co-Co exchange coupling as well. Overall this effect leads to a nearly 20% increase of  $T_C$ , with a maximum of 950 K at  $x = 0.2-0.23$ . This qualitatively confirms the experimentally observed trend. We find that further addition of Fe atoms is detrimental for the ferromagnetism in these alloys and  $T_C$  starts to decrease. Finally, we also find from theory that a large increase of  $T_C$  by nearly 35% can be obtained when Ce atoms are replaced by Y atoms in  $\text{CeCo}_5$  alloys.

### B. Multiscale modeling

In this section we present theoretical studies of the hysteretic behavior of Cu- and Ta-doped  $\text{CeCo}_5$  crystals to better understand the mechanism of coercivity in these systems. The physics of magnetic hysteresis involves multiple length scales and is controlled by both intrinsic and extrinsic properties of magnets. Therefore, our method is based on a multiscale approach that combines first-principles electronic structure calculations, micromagnetic models, and statistical macromagnetic simulations.

The electronic structure calculations describe material behavior on atomic length scales and allow us to evaluate intrinsic properties such as spontaneous magnetization and MAE. We use DFT within the rotationally invariant

DFT+ $U$  method [66] and the Perdew-Burke-Ernzerhof approximation for the exchange-correlation functional [71]. We use a Hubbard  $U$  of 2 eV and  $J = 0.8$  eV for Co 3d electrons, which were previously demonstrated to provide a good description of magnetic properties for  $\text{LaCo}_5$  and  $\text{YCo}_5$  materials [72]. The Kohn-Sham equations are solved by the projector-augmented-wave method [73] as implemented in the VIENNA AB INITIO SIMULATION PACKAGE [74,75]. We use a  $1 \times 1 \times 2$  supercell with respect to the primitive unit cell for  $\text{CeCo}_5$ . For the Brillouin-zone sampling the Monkhorst-Pack scheme [76] is used with a dense  $16 \times 16 \times 10$   $k$  mesh. The energy cutoff for the plane-wave expansion is set to 320 eV. The crystal structures are fully relaxed until forces acting on each atom are smaller than  $0.01$  eV/Å and all stress-tensor elements are smaller than 1 kbar. The MAE is evaluated with use of the force theorem as the total energy difference between states with the magnetization aligned along the [100] and [001] directions.

Figure 18 (top right) shows the calculated spontaneous magnetization and MAE for  $\text{Ce}(\text{Co}_{1-x}\text{Cu}_x)_5$  as a function of Cu content. We assume that the Cu atoms occupy the 3g atomic sites and we chose the lowest-energy atomic configurations that correspond to the Cu atoms occupying the same atomic layers. As seen, the spontaneous magnetization decreases with Cu content since Cu atoms have negligible moments as expected from their  $3d^{10}$  nominal configuration. This is in agreement with the experimental results shown in Fig. 15 (inset). Our calculations show that the MAE has a complex nonmonotonic dependence on Cu content. In particular, whereas small Cu additions decrease the MAE, for larger concentrations the MAE shows a maximum as a function of  $x$ . Converting these

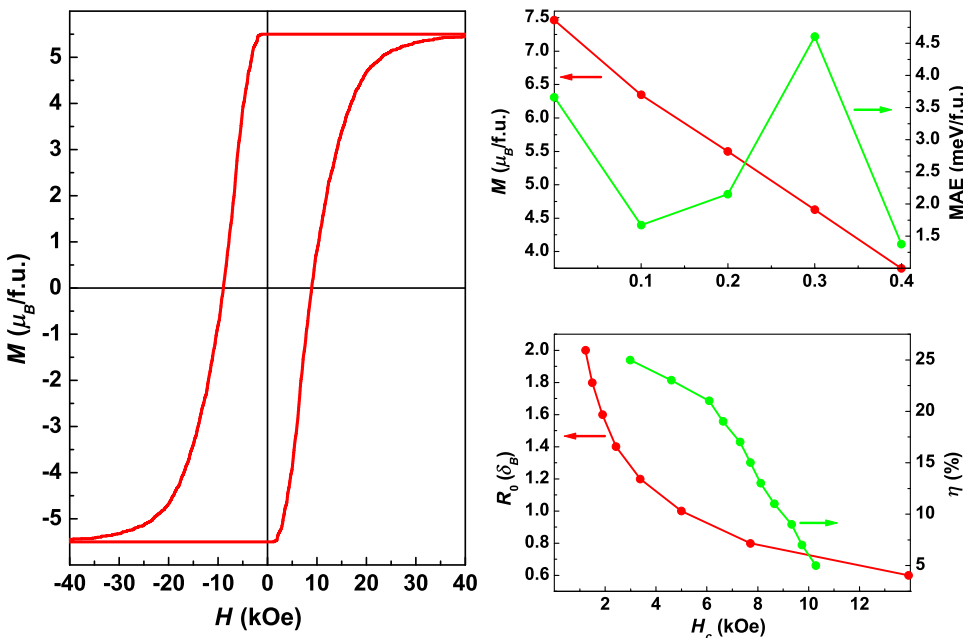


FIG. 18. Hysteresis loop of the  $\text{Ce}(\text{Co}_{0.8}\text{Cu}_{0.2})_5$  system (i.e.,  $\text{Ce}_{16.67}\text{Co}_{66.67}\text{Cu}_{16.67}$ ) calculated with  $\eta = 15\%$  and  $R_0 = 0.8\delta_B$  (left). The parameter  $\eta$  represents the probability of neighboring blocks to be exchange coupled, while  $R_0$  is the defect size, in the unit of the Bloch-wall thickness  $\delta_B$ , taken here as 4 nm [36]. Calculated spontaneous magnetization and MAE of  $\text{Ce}(\text{Co}_{1-x}\text{Cu}_x)_5$  ( $\text{Ce}_{16.67}\text{Co}_{83.33(1-x)}\text{Cu}_{83.33x}$ ) (i.e., as a function of Cu concentration) (top right). Coercivity of the  $\text{Ce}(\text{Co}_{0.8}\text{Cu}_{0.2})_5$  system (i.e., as a function of  $R_0$  and  $\eta$ ) (bottom right). The  $\eta$  ( $R_0$ ) dependence is evaluated for fixed  $R_0 = 0.8$  ( $\eta = 15\%$ ). f.u., formula unit.

calculated MAE and magnetization results to anisotropy fields  $H_a$ , we find the following anisotropy fields for  $x = 0, 0.1, 0.2, 0.3,$  and  $0.4$ , respectively: 166, 93, 131, 338, and 128 kOe. This nonmonotonic  $H_a$  behavior is qualitatively consistent with the experimental results for the anisotropy field as a function of Cu content shown in Fig. 12 except that, experimentally, the  $H_a$  maximum is observed at lower Cu content (approximately  $x = 0.2$  vs  $x = 0.3$  for the theory) and the corresponding  $H_a$  values differ significantly from the theoretical values. These differences are probably primarily caused by the fact that the configuration of Cu atoms in real samples differs in some respect from the lowest-energy configuration used in the calculations.

To study the hysteresis process, in addition to the knowledge of the intrinsic parameters (magnetic anisotropy and magnetization) as calculated above, we need to also specify the microstructural features of the system at the nanometer and micron length scales. As discussed in previous sections, SEM and STEM measurements indicate that a network of planar defects is present in the single-crystal samples. For the as-grown crystals these defects form Co-enriched and Cu-depleted laminar regions, which after heat treatment become nucleation points for Ta-rich planar precipitates. Clearly, these extended defects play a crucial role in establishing coercivity in the system since they can efficiently pin the reversed magnetic domains, thus preventing them from expanding over the entire crystal. As seen in Fig. 3, the crystal can be viewed as a collection of blocks (of the size of several microns) that are, to a large degree, magnetically decoupled by the planar defects. In our model we consider an idealized version of such a microstructure in the form of a simple cubic lattice of identical cubic micron-sized  $\text{Ce}(\text{Co}_{1-x}\text{Cu}_x)_5$  blocks. While the actual microstructure “blocks” are generally hexagonal (see Fig. 3), the use of a simple cubic lattice greatly simplifies the calculation and is not expected to drastically change the qualitative features. We assume periodic boundary conditions in a closed magnetic circuit setup so that there is no demagnetization field. Since the decoupling of blocks by the planar defects is not perfect, we introduce the parameter  $\eta$ , which physically represents the probability of neighboring blocks to be exchange coupled.

In addition, the blocks interact via the magnetostatic interaction, which is described with use of the Ewald technique as detailed in Ref. [77]. In a manner similar to the approach in Ref. [78], we assume that each block has a number of magnetically soft defects (e.g., Co precipitates) with exponentially distributed sizes  $f(R) = (1/R_0)e^{-R/R_0}$ , where  $R_0$  is the characteristic defect size. Assuming well-separated spherical defects, the switching field of each block can be determined by micromagnetic calculations using the intrinsic parameters (magnetic anisotropy and magnetization) calculated from the first-principles calculations above. The hysteresis loop is then calculated by our starting from the saturated state and gradually decreasing

the external magnetic field. For each value of the external field, the system magnetization is determined as follows. The total magnetic field acting on each block is evaluated as a sum of the external and magnetostatic contributions. When the total field is lower than the negative switching field of the block, the block magnetization is reversed. Subsequently, all blocks that are exchange coupled to the reversed block also have their magnetization reversed. The process is repeated iteratively until a stable magnetic configuration is achieved.

Figure 18 (left) shows the calculated hysteresis loop for a  $\text{Ce}(\text{Co}_{0.8}\text{Cu}_{0.2})_5$  system calculated with  $\eta = 15\%$  and  $R_0 = 0.8\delta_B$ , where  $\delta_B$  is the Bloch-wall thickness of  $\text{CeCo}_5$  (around 4 nm [36]). As is evident, this choice of parameters result in a rectangular hysteresis loop with a coercivity similar to the measured value for this Co content (see Fig. 15). Therefore, our model is capable of reproducing the experimental results. Figure 18 (bottom right) shows the dependence of the coercivity on the microstructural parameters:  $\eta$  and  $R_0$ . We observe that for  $R_0 < \delta_B$ ,  $R_0$  strongly affects the coercivity, while for  $R_0 > \delta_B$ , the coercivity depends only weakly on  $R_0$ . As expected, the coercivity decreases with  $\eta$ . Around  $\eta = 20\%$  we observe a change of slope and a much-stronger reduction of coercivity is observed for larger  $\eta$ . These results indicate that there are two possible mechanisms by which Cu doping enhances the coercivity. First, Cu doping may increase the number and thickness of planar defects, resulting in a decrease of  $\eta$ . This is consistent with a scenario in which the defects are precipitates of the Cu-poor 1:5 phase. A second possibility is that the Cu doping reduces the size of the magnetically soft defects in the matrix phase.

## VI. CONCLUSIONS

Using a self-flux technique, we synthesize five different single crystals of Ta-, Cu- and/or Fe-substituted  $\text{CeCo}_5$ . They retain a  $\text{CaCu}_5$  substructure and incorporate small amounts of Ta in the form of “dumbbells” filling the  $2e$  crystallographic sites within the 1D hexagonal channel with the  $1a$  Ce site, whereas Co, Cu, and Fe are statistically distributed among the  $2c$  and  $3g$  crystallographic sites. The as-grown crystals appear to be single phased and homogeneous in composition. Their single crystallinity is confirmed by XRD, SEM, and TEM experiments. However, they also exhibit significant magnetic coercivities that are comparable to those of most anisotropic sintered alnico grades. After the heat treatment (hardening), magnetic characteristics significantly improve. Ta atoms leave the matrix interstices of the as-grown crystals and precipitate in form of coherent laminas, creating the so-called composite crystal. The composite crystal, formed during the heat treatment, contains a 3D array of structural defects within a primarily single-grain single crystal. The mechanism of coercivity is regulated by Cu, and



pinning occurs on the extended 3D defects and structural imperfections that originate from Cu-depleted and Co-enriched lines observed in the as-grown crystals and consequently develop into the regions between Ta-rich precipitates and the matrix in the thermally aged crystals. The structural defects form as a result of a thermodynamic transformation of the matrix material associated with its partial decomposition and/or decreased miscibility during the hardening process. Significant increase of magnetization in the heat-treated samples may be associated either with the transformation of the matrix phase or with the removal of Ta from the matrix. Fe strongly increases both the Curie temperature and magnetization of the system, which is associated with a strong increase in the magnetic ordering energy. The peculiar thermodynamic transformations, which lead to intragranular pinning and a unique coercivity mechanism that does not require the typical processing for the development of extrinsic magnetic properties, could be used to create permanent magnets with lowered processing costs. Further composition-temperature-time optimizations may result in a critical-material-free and cost-efficient gap magnet with energy product 15–16.5 MGOe.

### ACKNOWLEDGMENTS

This research was supported by the Critical Materials Institute, an Energy Innovation Hub funded by the U.S. Department of Energy, Office of Energy Efficiency and Renewable Energy, Advanced Manufacturing Office. M.C.N. is supported by the Office of Basic Energy Sciences, Materials Sciences Division, U.S. Department of Energy. This work was performed at the Ames Laboratory, operated for the U.S. Department of Energy by Iowa State University under Contract No. DE-AC02-07CH11358.

- 
- [1] G. B. Haxel, J. B. Hendrick, and G. J. Orris Demagnetizing factors for rectangular ferromagnetic prisms, U.S. Geological Survey Fact Sheet (2002).
- [2] Pradyot Patnaik, *Handbook of Inorganic Chemicals* (McGraw-Hill Professional, New York, 2002).
- [3] Feng Xie, Ting An Zhang, David Dreisinger, and Fiona Doyle, A critical review on solvent extraction of rare earths from aqueous solutions, *Miner. Eng.* **56**, 10 (2014).
- [4] J. F. Herbst, J. J. Croat, and W. B. Yelon, Structural and magnetic properties of Nd<sub>2</sub>Fe<sub>14</sub>B (invited), *J. Appl. Phys.* **57**, 4086 (1985).
- [5] Arjun K. Pathak, Mahmud Khan, Karl A. Gschneidner, Ralph W. McCallum, Lin Zhou, Kewei Sun, Kevin W. Dennis, Chen Zhou, Frederick E. Pinkerton, Matthew J. Kramer, and Vitalij K. Pecharsky, Cerium: An unlikely replacement of dysprosium in high performance Nd<sub>2</sub>Fe<sub>14</sub>B permanent magnets, *Adv. Mater.* **27**, 2663 (2015).
- [6] Arjun K. Pathak, K. A. Gschneidner, M. Khan, R. W. McCallum, and V. K. Pecharsky, High performance Nd-Fe-B permanent magnets without critical elements, *J. Alloys. Compd.* **668**, 80 (2016).
- [7] Michael A. Susner, Benjamin S. Conner, Bayrammurad I. Saparov, Michael A. McGuire, Ethan J. Crumlin, Gabriel M. Veith, Huibo Cao, Kavungal V. Shanavas, David S. Parker, Bryan C. Chakoumakos, and Brian C. Sales, Flux growth and characterization of Ce-substituted Nd<sub>2</sub>Fe<sub>14</sub>B single crystals, *J. Magn. Magn. Mater.* **434**, 1 (2017).
- [8] Karl J. Strnat, and Reinhold M. W. Strnat, Rare earth-cobalt permanent magnets, *J. Magn. Magn. Mater.* **100**, 38 (1991).
- [9] H. Senno, and Y. Tawara, Permanent-magnet properties of Sm-Ce-Co-Fe-Cu alloys with compositions between 1–5 and 2–17, *IEEE Trans. Magn.* **10**, 313 (1974).
- [10] M. J. Kramer, R. W. McCallum, I. A. Anderson, and S. Constantinides, Prospects for non-rare earth permanent magnets for traction motors and generators, *JOM* **64**, 752 (2012).
- [11] R. W. McCallum, L. Lewis, R. Skomski, M. J. Kramer, and I. E. Anderson, Practical aspects of modern and future permanent magnets, *Annu. Rev. Mater. Res.* **44**, 451 (2014).
- [12] E. A. Nesbitt, New permanent magnet materials containing rare-earth metals, *J. Appl. Phys.* **40**, 1259 (1969).
- [13] E. A. Nesbitt, R. H. Willens, R. C. Sherwood, E. Buehler, and J. H. Wernick, New permanent magnet materials, *Appl. Phys. Lett.* **12**, 361 (1968).
- [14] Yoshio Tawara, and Harufumi Senno, Cerium, cobalt and copper alloy as a permanent magnet material, *Jpn J. Appl. Phys.* **7**, 966 (1968).
- [15] J. M. D. Coey, Permanent magnets: Plugging the gap, *Scr. Mater.* **67**, 524 (2012).
- [16] Harufumi Senno, and Yoshio Tawara, Microstructure of a cerium, cobalt and copper alloy with a high coercivity, *Jpn J. Appl. Phys.* **8**, 118 (1969).
- [17] E. A. Nesbitt, G. Y. Chin, R. C. Sherwood, and J. H. Wernick, Effect of processing on permanent magnet materials containing rare-earth metals, *J. Appl. Phys.* **40**, 4006 (1969).
- [18] Thomas J. Cullen, Cast permanent magnets of cobalt, copper, and cerium: Process and performance characteristics, *J. Appl. Phys.* **42**, 1535 (1971).
- [19] R. C. Sherwood, E. A. Nesbitt, G. Y. Chin, and M. L. Green, Preparation and properties of sintered CoCuFeCe permanent magnets, *Mater. Res. Bull.* **7**, 489 (1972).
- [20] Y. Tawara, and H. Senno, Sintered magnets of copper-and iron-modified cerium cobalt, *IEEE Trans. Magn.* **8**, 560 (1972).
- [21] G. Chin, M. Green, E. Nesbitt, R. Sherwood, and J. Wernick, Directional solidification of Co-Cu-R permanent-magnet alloys, *IEEE Trans. Magn.* **8**, 29 (1972).
- [22] E. A. Nesbitt, G. Y. Chin, G. W. Hull, R. C. Sherwood, M. L. Green, J. H. Wernick, Hugh C. Wolfe, C. D. Graham, and J. J. Rhyne, in *AIP Conference Proceedings* (AIP, Denver, Colorado, 1973).
- [23] H. Leamy, and M. Green, The structure of Co-Cu-Fe-Ce permanent magnets, *IEEE Trans. Magn.* **9**, 205 (1973).
- [24] E. Nesbitt, G. Chin, R. Sherwood, M. Green, and H. Leamy, Influence of cerium content on the structure and magnetic behavior of Co-Fe-Cu-Ce permanent magnets, *IEEE Trans. Magn.* **9**, 203 (1973).
- [25] Y. Khan, Intermetallic compounds in the cobalt-rich part of the R-cobalt systems (R = Ce, La, Ce-La), *J. Less Common Met.* **34**, 191 (1974).

- [26] M. P. Arbuzov, A. A. Pavlyukov, and A. G. Leskevich, Coercive force of cast and sintered permanent magnets in Co-Cu-Fe-Ce alloys, *Poroshk. Metall.* **9**, 48 (1974).
- [27] M. P. Arbuzov, A. A. Pavlyukov, and A. G. Pogorilyy, X-ray diffraction analysis of the phase composition of the alloy  $\text{Co}_4\text{CuCe}_{1.02}$ , *Fiz. Metal. Metalloved.* **40**, 848 (1975).
- [28] M. P. Arbuzov, A. A. Pavlyukov, A. G. Pogorilyi, and O. S. Opanasenko, Crystal structure and coercive force of sintered permanent magnets in alloys of the system Co-Cu-Fe-Ce, *Poroshk. Metall.* **5**, 97 (1975).
- [29] M. P. Arbuzov, A. A. Pavlyukov, E. V. Krakovich, and O. S. Opanasenko, Magnetic characteristics of sintered permanent magnets in  $(\text{Co}, \text{Cu}, \text{Fe})_5\text{Ce}$  alloys, *Poroshk. Metall.* **7**, 56 (1977).
- [30] M. P. Arbuzov, A. A. Pavlyukov, E. V. Krakovich, and O. S. Opanasenko, Magnetic characteristics of sintered permanent magnets in alloys of the Co-Cu-Fe-Ce system, *Poroshk. Metall.* **8**, 69 (1977).
- [31] M. P. Arbuzov, A. A. Pavlyukov, E. V. Krakovich, and O. S. Opanasenko, Magnetic properties of sintered  $(\text{Co}, \text{Cu}, \text{Fe})_5\text{Ce}$  alloys, *Poroshk. Metall.* **9**, 85 (1977).
- [32] Koichiro Inomata, Teruo Oshima, Tadashi Ido, and Masakazu Yamada, Sintered Ce-Co-Cu-Fe-Ti magnets, *Appl. Phys. Lett.* **30**, 669 (1977).
- [33] Yoshio Tawara, Tetsuichi Chino, and Yukihiko Matsui, Permanent magnets based on  $(\text{Ce}, \text{Sm})(\text{Co}, \text{Fe}, \text{Cu})_2$ , *Appl. Phys. Lett.* **33**, 674 (1978).
- [34] B. Labulle, and C. Petipas, X-ray study of monocrystalline alloys near the composition  $\text{CeCo}_{3.5}\text{Cu}_{1.5}$ , *J. Less Common Met.* **66**, 183 (1979).
- [35] B. Labulle, and C. Petipas, Oxidation study of monocrystalline  $\text{CeCo}_{5-x}\text{Cu}_x$  by X-ray diffraction methods, *J. Less Common Met.* **71**, 183 (1980).
- [36] D. Girodin, C. H. Allibert, F. Givord, and R. Lemaire, Phase equilibria in the  $\text{CeCo}_5\text{-CeCu}_5$  system and structural characterization of the  $(\text{CeCo}_{1-x}\text{Cu}_x)_5$  phases, *J. Less Common Met.* **110**, 149 (1985).
- [37] H. Okamoto, in *Ce-Co Phase Diagram, ASM Alloy Phase Diagrams Database*, P. Villars editor-in-chief, H. Okamoto and K. Cenoz, section editors (ASM International, Materials Park, OH, 2006).
- [38] P. C. Canfield, and Z. Fisk, Growth of single crystals from metallic fluxes, *Philos. Mag.* **65**, 1117 (1992).
- [39] P. C. Canfield, in *Properties and Applications of Complex Intermetallics, Solution Growth of Intermetallic Single Crystals: A Beginner Guide*, edited by Belin-Ferre (World Scientific, Singapore, 2010), Chap. 2.
- [40] Paul C. Canfield, and Ian R. Fisher, High-temperature solution growth of intermetallic single crystals and quasicrystals, *J. Crystal Growth* **225**, 155 (2001). Proceedings of the 12th American Conference on Crystal Growth and Epitaxy.
- [41] Juan Rodríguez-Carvajal, Recent advances in magnetic structure determination by neutron powder diffraction, *Phys. B: Condens. Matter* **192**, 55 (1993).
- [42] SMART (Bruker AXS Inc., Madison, Wisconsin, 1996).
- [43] SHELXTL (Bruker AXS Inc., Madison, Wisconsin, 2000).
- [44] R. H. Blessing, An empirical correction for absorption anisotropy, *Acta Crystallogr. Sect. A: Found. Crystallogr.* **51**, 33 (1995).
- [45] See Supplemental Material at <http://link.aps.org/supplemental/10.1103/PhysRevApplied.11.014052> for crystal information files and checkCIF reports.
- [46] Tej N. Lamichhane, Valentin Taufour, Srinivasa Thimmaiah, David S. Parker, Sergey L. Bud'ko, and Paul C. Canfield, A study of the physical properties of single crystalline  $\text{Fe}_5\text{B}_2\text{P}$ , *J. Magn. Magn. Mater.* **401**, 525 (2016).
- [47] Tej N. Lamichhane, Valentin Taufour, Andriy Palasyuk, Qisheng Lin, Sergey L. Bud'ko, and Paul C. Canfield,  $\text{Ce}_{3-x}\text{Mg}_x\text{Co}_9$ : Transformation of a Pauli Paramagnet into a Strong Permanent Magnet, *Phys. Rev. Appl.* **9**, 024023 (2018).
- [48] O. Bodak, Ya Tokaychuk, M. Manyako, V. Pacheco, R. Cerný, and K. Yvon, Structural and magnetic properties of iron-rich compounds in the Yb-Fe-Al system, *J. Alloys. Compd.* **354**, L10 (2003).
- [49] Ya. O. Tokaychuk, O. I. Bodak, Yu. K. Gorelenko, and K. Yvon, Structural and magnetic properties of iron-rich compounds in the Yb-Fe-Ga system, *J. Alloys. Compd.* **415**, 8 (2006).
- [50] Radovan Černý, Yaroslav Filinchuk, and Stefan Bruehne, Local atomic order in the vicinity of  $\text{Cu}_2$  dumbbells in  $\text{TbCu}_7$ -type  $\text{YCu}_{6.576}$  studied by Bragg and total scattering techniques, *Intermetallics* **17**, 818 (2009).
- [51] K. H. J. Buschow, and A. S. van der Goot, Composition and crystal structure of hexagonal Cu-rich rare earth-copper compounds, *Acta Crystallogr. Sect. B: Struct. Crystallogr. Crystal Chem.* **27**, 1085 (1971).
- [52] I. S. Vinogradova, and E. S. Makarov, The crystal structure of  $\text{Th}_2\text{Zn}_{17}$  and  $\text{U}_2\text{Zn}_{17}$ , *Kristallografiya* **1**, 634 (1956).
- [53] J. V. Florio, N. C. Baenziger, and R. E. Rundle, Compounds of thorium with transition metals. II. Systems with iron, cobalt and nickel, *Acta Crystallogr.* **9**, 367 (1956).
- [54] D. Givord, R. Lemaire, J. M. Moreau, and E. Roudaut, X-ray and neutron determination of a so-called 1:7-type structure in the lutetium-iron system, *J. Less-Comm. Met.* **29**, 361 (1972).
- [55] K. H. J. Buschow, The crystal structures of the rare-earth compounds of the form  $\text{R}_2\text{Ni}_{17}$ ,  $\text{R}^2\text{Co}_{17}$  and  $\text{R}_2\text{Fe}_{17}$ , *J. Less Common Met.* **11**, 204 (1966).
- [56] Chen Zhou, Frederick E. Pinkerton, and Jan F. Herbst, Formation of  $\text{TbCu}_7$ -type  $\text{CeFe}_{10}\text{Zr}_{0.8}$  by rapid solidification, *J. Alloys. Compd.* **569**, 6 (2013).
- [57] M. I. Bartashevich, T. Goto, R. J. Radwanski, and A. V. Korolyov, Magnetic anisotropy and high-field magnetization process of  $\text{CeCo}_5$ , *J. Magn. Magn. Mater.* **131**, 61 (1994).
- [58] W. Sucksmith, and J. E. Thompson, The magnetic anisotropy of cobalt, *Proc. R. Soc. London A: Math. Phys. Eng. Sci.* **225**, 362 (1954).
- [59] Valentin Taufour, Srinivasa Thimmaiah, Stephen March, Scott Saunders, Kwei Sun, Tej Nath Lamichhane, Matthew J. Kramer, Sergey L. Bud'ko, and Paul C. Canfield, Structural and Ferromagnetic Properties of an Orthorhombic Phase of MnBi Stabilized with Rh Additions, *Phys. Rev. Appl.* **4**, 014021 (2015).
- [60] P. R. Bevington, and D. K. Robinson, *Data reduction and error analysis for the physical sciences* (McGraw-Hill, New York, 2003).

- [61] Standard specifications for permanent magnet materials (MMPA standard no. 0100-00).
- [62] Lars Nordström, Olle Eriksson, M. S. S. Brooks, and Börje Johansson, Theory of ferromagnetism in  $\text{CeCo}_5$ , *Phys. Rev. B* **41**, 9111 (1990).
- [63] A. J. Manuel, and J. M. P. S. Quinton, The magnetic susceptibilities of palladium and palladium-rhodium alloys from 1.85 to 293 K, *Proc. R. Soc. A: Math. Phys. Eng. Sci.* **273**, 412 (1963).
- [64] P. Blaha, K. Schwarz, G. Madsen, D. Kvasnicka, and J. Luitz, An augmented plane wave plus local orbitals program for calculating crystal properties (2001).
- [65] V. I. Anisimov, I. V. Solovyev, M. A. Korotin, M. T. Czyżyk, and G. A. Sawatzky, Density-functional theory and NiO photoemission spectra, *Phys. Rev. B* **48**, 16929 (1993).
- [66] A. I. Liechtenstein, V. I. Anisimov, and J. Zaanen, Density-functional theory and strong interactions: Orbital ordering in Mott-Hubbard insulators, *Phys. Rev. B* **52**, R5467 (1995).
- [67] Lars Nordstroem, Olle Eriksson, M. S. S. Brooks, and Beorje Johansson, Theory of ferromagnetism in  $\text{CeCo}_5$ , *Phys. Rev. B* **41**, 9111 (1990).
- [68] A. I. Liechtenstein, M. I. Katsnelson, V. P. Antropov, and V. A. Gubanov, Local spin density functional approach to the theory of exchange interactions in ferromagnetic metals and alloys, *J. Magn. Magn. Mater.* **67**, 65 (1987).
- [69] V. P. Antropov, B. N. Harmon, and A. N. Smirnov, Aspects of spin dynamics and magnetic interactions, *J. Magn. Magn. Mater.* **200**, 148 (1999).
- [70] I. A. Zhuravlev, V. P. Antropov, and K. D. Belashchenko, Spin-Fluctuation Mechanism of Anomalous Temperature Dependence of Magnetocrystalline Anisotropy in Itinerant Magnets, *Phys. Rev. Lett.* **115**, 217201 (2015).
- [71] John P. Perdew, Kieron Burke, and Matthias Ernzerhof, Generalized Gradient Approximation Made Simple, *Phys. Rev. Lett.* **77**, 3865 (1996).
- [72] Manh Cuong Nguyen, Yongxin Yao, Cai-Zhuang Wang, Kai-Ming Ho, and Vladimir P. Antropov, Magnetocrystalline anisotropy in cobalt based magnets: A choice of correlation parameters and the relativistic effects, *J. Phys.: Condens. Matter* **30**, 195801 (2018).
- [73] P. E. Blochl, Projector augmented-wave method, *Phys. Rev. B* **50**, 17953 (1994).
- [74] G. Kresse, and J. Furthmüller, Efficient iterative schemes for ab initio total-energy calculations using a plane-wave basis set, *Phys. Rev. B* **54**, 11169 (1996).
- [75] G. Kresse, and D. Joubert, From ultrasoft pseudopotentials to the projector augmented-wave method, *Phys. Rev. B* **59**, 1758 (1999).
- [76] Hendrik J. Monkhorst, and James D. Pack, Special points for Brillouin-zone integrations, *Phys. Rev. B* **13**, 5188 (1976).
- [77] Aleksander L. Wysocki, and Vladimir P. Antropov, Micro-magnetic simulations with periodic boundary conditions: Hard-soft nanocomposites, *J. Magn. Magn. Mater.* **428**, 274 (2017).
- [78] R. Blank, What determines the demagnetization in Nd-Fe-B magnets? *J. Magn. Magn. Mater.* **101**, 317 (1991).